TU Delft

Delft University of Technology

Integrated Design Optimization of Environmental Control Systems for Next-Generation Aircraft

Giuffre, Andrea; Ascione, Federica; Colonna, Piero; De Servi, Carlo

DOI
10.2514/1.C038093

Publication date
2025

Document Version
Final published version

Published in
Journal of Aircraft

Citation (APA)
Giuffre, A., Ascione, F., Colonna, P., & De Servi, C. (2025). Integrated Design Optimization of Environmental Control Systems for Next-Generation Aircraft. *Journal of Aircraft*, *62*(3), 498-516. https://doi.org/10.2514/1.C038093

Important note
To cite this publication, please use the final published version (if applicable).
Please check the document version above.

Copyright
Other than for strictly personal use, it is not permitted to download, forward or distribute the text or part of it, without the consent of the author(s) and/or copyright holder(s), unless the work is under an open content license such as Creative Commons.

Takedown policy
Please contact us and provide details if you believe this document breaches copyrights.
We will remove access to the work immediately and investigate your claim.

This work is downloaded from Delft University of Technology.
For technical reasons the number of authors shown on this cover page is limited to a maximum of 10.

Green Open Access added to TU Delft Institutional Repository
as part of the Taverne amendment.

More information about this copyright law amendment
can be found at https://www.openaccess.nl.

Otherwise as indicated in the copyright section:
the publisher is the copyright holder of this work and the
author uses the Dutch legislation to make this work public.

JOURNAL OF AIRCRAFT
Vol. 62, No. 3, May–June 2025

Integrated Design Optimization of Environmental Control Systems for Next-Generation Aircraft

Andrea Giuffre',* Federica Ascione,† Piero Colonna,‡ and Carlo De Servi§
Delft University of Technology, 2629 HS Delft, The Netherlands

https://doi.org/10.2514/1.C038093

The use of an electrically driven vapor compression cycle (VCC) for the environmental control system (ECS) of next-generation aircraft could substantially reduce fuel consumption. The renovated interest in this technology is due to the advent of new refrigerants featuring low global warming potential and the latest developments in high-speed centrifugal compressors and ultracompact heat exchangers. This paper documents the development of an integrated design optimization method for aircraft ECS, whereby the system-level design is performed along with the preliminary design of its main components. The methodology is used to perform the multipoint and multi-objective design optimization of a bleedless air cycle machine (ACM), i.e., the state-of-the-art ECS installed onboard the Boeing 787, and an electrically driven VCC system for a single-aisle, short-haul aircraft. The performance of the two optimal architectures is compared, showing that the VCC system is characterized by lower weight and electric power consumption than the bleedless ACM but features a higher drag penalty. Overall, the optimal VCC system leads to an 18% reduction in fuel weight penalty with respect to the bleedless ACM for the prescribed application.

Nomenclature

A	=	area, m^2
b	=	fins height, m
C_r	=	heat capacity ratio
C_D	=	drag coefficient
C_P	=	pressure recovery factor
D	=	drag, N
D_{hyd}	=	hydraulic diameter, m
F_{ax}	=	axial thrust, N
F_d, F_p	=	flow depth and fins pitch, m
f	=	friction factor
G	=	mass flux, $kg \cdot m^{-2} \cdot s^{-1}$
H	=	blade height, m
h	=	specific enthalpy, $J \cdot kg^{-1}$
h_{conv}	=	heat transfer coefficient, $W \cdot m^{-2} \cdot K^{-1}$
j	=	Colburn factor
k	=	impeller shape factor
λ	=	thermal conductivity, $W \cdot m^{-1} \cdot K^{-1}$
L	=	lift, N
L_p, L_l, L_h	=	louver pitch, louver length, and louver height, m
l_f, l_t	=	fin length and tube length, m
NTU	=	number of transfer units
OR	=	operating range
p	=	pitch, m
P	=	pressure, Pa, and power, W
P_{el}	=	electric power, W
P_m	=	mechanical power, W
P_t	=	tubes pitch, m
Pr	=	Prandtl number
R	=	radius, m
Re	=	Reynolds number
R_{th}	=	thermal resistance, k/W
SFC_P	=	power specific fuel consumption, $lb \cdot h^{-1} \cdot hp^{-1}$
SFC_{th}	=	thrust specific fuel consumption, $lb \cdot h^{-1} \cdot lbf^{-1}$
t	=	thickness, m
T	=	temperature, K
T_h	=	tube height, m
U	=	overall heat transfer coefficient, $W \cdot m^{-2} \cdot K^{-1}$
U_2	=	impeller peripheral speed, $m \cdot s^{-1}$
v	=	velocity, $m \cdot s^{-1}$
V	=	volume, m^3
W	=	weight, kg
W_{f0}	=	fuel weight penalty, kg
x, y, z	=	core width, core height, and core depth, m
α	=	flow angle, rad
β	=	pressure ratio
δ	=	thickness, m
ϵ	=	effectiveness
η	=	efficiency
Θ	=	louver angle, rad
κ_s	=	splitting factor
ρ	=	density, $kg \cdot m^{-3}$
τ	=	aircraft mission time, s
ϕ_{t1}	=	swallowing capacity
ψ_{is}	=	isentropic loading coefficient
Ω	=	rotational speed, $rad \cdot s^{-1}$

Subscripts

bl	=	impeller blade
cond	=	condensation
cr	=	cruise operating point
el	=	electrical
eva	=	evaporation
f	=	fins
ff	=	free-flow
fl	=	flush intake
fp	=	faulty pack operating point
hg	=	hot ground operating point
is	=	isentropic
mc	=	microchannel
p	=	plates
pp	=	pinch point
s1, s2	=	first and second compressor stages
sc, sh	=	subcooling and superheating
t	=	tubes

Received 10 June 2024; accepted for publication 8 November 2024; published online Open Access 21 February 2025. Copyright © 2025 by the American Institute of Aeronautics and Astronautics, Inc. All rights reserved. All requests for copying and permission to reprint should be submitted to CCC at www.copyright.com; employ the eISSN 1533-3868 to initiate your request. See also AIAA Rights and Permissions www.aiaa.org/randp.

*Guest Researcher, Propulsion and Power, Faculty of Aerospace Engineering; also Elysian Aircraft, 3641 SK Mijdrecht, The Netherlands.

†Post-Doctoral Researcher, Propulsion and Power, Faculty of Aerospace Engineering.

‡Full Professor and Chair, Propulsion and Power, Faculty of Aerospace Engineering.

§Senior Researcher, Propulsion and Power, Faculty of Aerospace Engineering; also Flemish Institute for Technological Research (VITO), 2400 Mol, Belgium; c.m.deservi@tudelft.nl.

Downloaded by Technische Universiteit Delft on July 17, 2025 | http://arc.aiaa.org | DOI: 10.2514/1.C038093

tt = total-to-total
1, 2, 3, 4 = impeller inlet, impeller outlet, diffuser outlet, and volute outlet
w = wall

I. Introduction

THE environmental control system (ECS) is the largest user of nonpropulsive power onboard aircraft, accounting for up to 3–5% of the total fuel burn [1]. To reduce the fuel consumption due to the ECS, the Boeing 787 has been equipped with a bleedless air cycle machine (ACM) driven by an electrical motor. This solution eliminates the extraction of pneumatic power generated by the engines and enables a reduction of specific fuel consumption in the range of 1–2% at cruise conditions [2]. In addition to fuel savings, adopting an electrically powered ECS is expected to reduce maintenance costs and increase system reliability due to the removal of the maintenance-intensive bleed system [2,3]. Furthermore, the replacement of the traditional ACM architecture, based on the inverse Brayton cycle, with a vapor compression cycle (VCC) system may lead to a substantial reduction of the electric power consumption. However, the adoption of this technology in the aerospace sector has been historically very limited due to safety concerns and regulations regarding the ozone-depleting potential (ODP), toxicity, and flammability of the working fluids used as refrigerants, as well as because of the larger weight associated with VCC systems, which are commonly designed for stationary applications. However, with the advent of next-generation refrigerants, featuring low global warming potential (GWP), together with the recent development of high-speed centrifugal compressors and ultracompact heat exchangers, there is renovated interest in the possibility of adopting VCC systems for airborne applications.

A dynamic model for the simulation of both steady-state and transient operations of VCC systems for aircraft ECS was developed and is documented in [4]. The authors state that the main efforts were focused on the development of two-phase heat exchanger models, whereas the performance of other components, e.g., the refrigerant compressor (RC), was calculated through look-up tables. The same model has been refined and applied to simulate the ECS operating envelope during the flight mission of an Airbus A320 on a hot day in [5]. The study demonstrates the feasibility of an electrically driven VCC system for commercial aircraft applications but does not show any performance comparisons with respect to the current state-of-the-art. Hu et al. [6] present a graph-theory steady-state model to investigate arbitrary layouts of the refrigeration cycle and the cooling fluid loop used for the thermal management of galleys and avionics of commercial aircraft. The model was validated experimentally, resulting in a difference between calculated and measured values of $\pm 8\%$ for the cooling capacity, $\pm 8°C$ for the system temperatures, and $\pm 10\%$ for the system pressures. The possibility of using a VCC system to heat the aircraft cabin in cold environments has been investigated experimentally by Xu et al. [7]. The authors proposed to integrate the VCC-based ECS with the engine oil lubrication loop through a refrigerant-oil heat exchanger. During normal operation of the ECS, the refrigerant-oil heat exchanger is bypassed and the two systems are decoupled. When cabin heating is required, the heat coming from the lubricating oil is used for the evaporation of the refrigerant, and the air at the outlet of the condenser is supplied to the cabin. From a more theoretical perspective, Yang and Yang [8] derived an analytical formulation of the COP for five different ACM configurations. However, the authors assumed dry air and ideal gas to obtain the explicit formulation of the COP, therefore hindering its application to VCC systems, in which the working fluid undergoes phase changes and does not obey the ideal gas law. In the aforementioned studies, the sizing and performance of the heat exchangers and turbomachines have not been accounted for within the conceptual design of the VCC system. However, as reported in [9], the performance of the ECS strongly depends on the characteristics of its components. Therefore, an integrated design approach, i.e., a computational framework in which the design variables of the system and those related to its main components are treated simultaneously, is arguably required to tackle the design optimization of the ECS.

Vargas and Bejan [10] documented a pioneering application of the integrated design philosophy to the optimization of a simplified ECS configuration. Following this study, numerous authors have attempted to apply the integrated design method to more complex and more realistic ECS layouts. The multi-objective optimization of a two-wheel bootstrap ACM has been addressed in [11]. The optimization targeted the minimization of the volume of the two offset strip fin heat exchangers and of the total entropy generation at cruise conditions. Subsequently, the study has been extended to include a thermo-economic analysis [12]. The multi-objective optimization of a hybrid ACM-VCC system operating under three different scenarios has been investigated by Sielemann et al. [13]. In a recent study, Li et al. [14] proposed a methodology they referred to as the heat current method to simplify the analysis and the optimization of a conventional ECS configuration. The multi-objective optimization of a three-wheel bootstrap ACM, including the high-pressure water separation loop, has been tackled by Duan et al. [15].

All the studies concerning the integrated design optimization of aircraft ECS targeted conventional or hybrid ACM configurations, focusing the modeling effort on the heat exchangers. However, the RC is arguably the most critical component of a VCC system because the compressor choke and stall margins directly affect the operating range of the system, and the COP is directly proportional to the compressor efficiency. Therefore, a model accounting for the preliminary design of the high-speed centrifugal compressor should be included in an integrated design framework for VCC-based ECS. A first attempt to develop and apply such methodology is documented in [16]. The authors performed an integrated design optimization of a VCC-based aircraft ECS, including the preliminary design of the high-speed centrifugal compressor, which has been modeled using a data-driven surrogate model. Another example of the application of such methodology for the design optimization of the ECS of a large rotorcraft is reported in [17]. Only one ECS configuration and one operating point have been considered in both studies. However, in real applications, the ECS is characterized by a broad operating envelope, ranging from cruise operation to extreme operating points, such as ground operation on a hot and humid day and flight operation in the presence of a faulty ECS pack. As a result, the optimal preliminary design of the system can be obtained only with a multipoint optimization strategy.

The objective of this work is therefore twofold. The first goal is to advance the state-of-the-art regarding the methodologies used for the integrated design optimization of aircraft ECS. This is achieved by demonstrating the capabilities of a new multi-objective and multipoint optimization framework, embedding the preliminary design of the compact heat exchangers, the cabin air compressor, and the RC within the system-level design. The second target is to compare the performance metrics of two optimized ECS configurations featuring different architectures: a bleedless three-wheel bootstrap ACM, i.e., the system equipping the Boeing 787, and an electrically driven VCC system powered by a twin-stage centrifugal compressor. The ultimate goal is to evaluate if the theoretical benefits of the envisaged novel ECS architecture can be realized. The remainder of the paper is structured as follows. First, the methodology used to model the main components of the two systems is introduced. Then, the structure of the optimization framework is presented. Next, the results of the bleedless ACM and the VCC system are discussed and compared. Finally, the main outcomes of this study are summarized in the form of concluding remarks, and an outlook for future work is provided.

II. Methodology

A. System Model

The models of the two ECS configurations have been implemented using the acausal [18], object-oriented, equation-based Modelica language. The models of the system components are included in the in-house Modelica library for the Design and Simulation of Energy Conversion Systems (DeSimECS). All the components are treated as steady-state and zero-dimensional and can be used without adaptations

Downloaded by Technische Universiteit Delft on July 17, 2025 | http://arc.aiaa.org | DOI: 10.2514/1.C038093

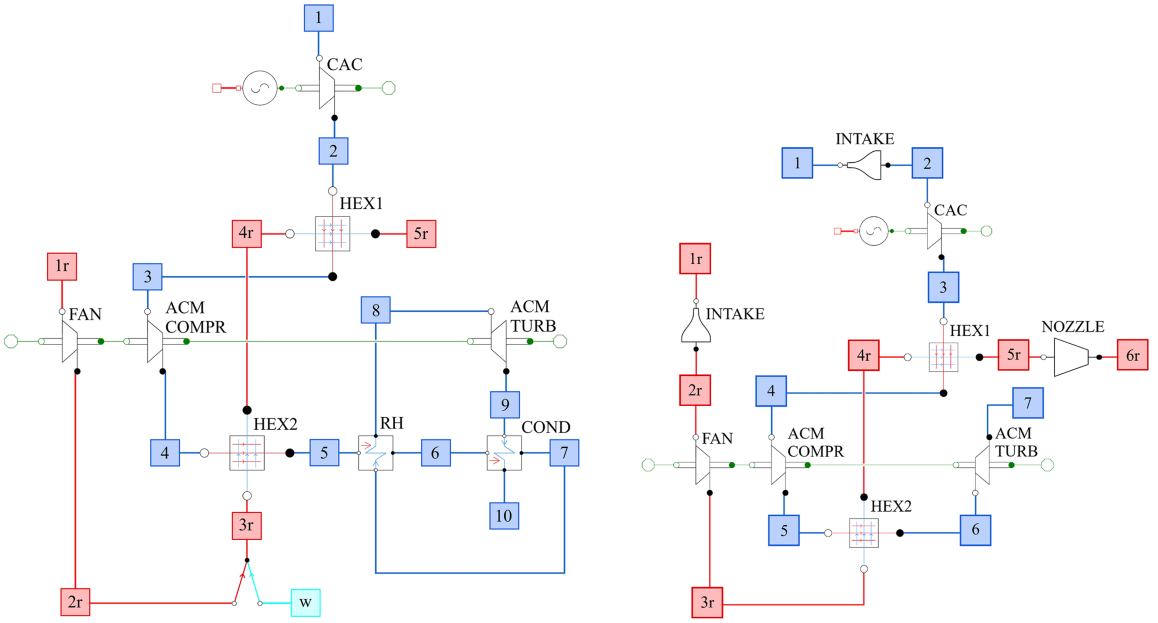

a) Model used to simulate ground operation b) Model used to simulate operation during flight

Fig. 1 Modelica models of the ACM. The thermodynamic states of the ram air stream and the cabin air stream are highlighted in red and blue, respectively.

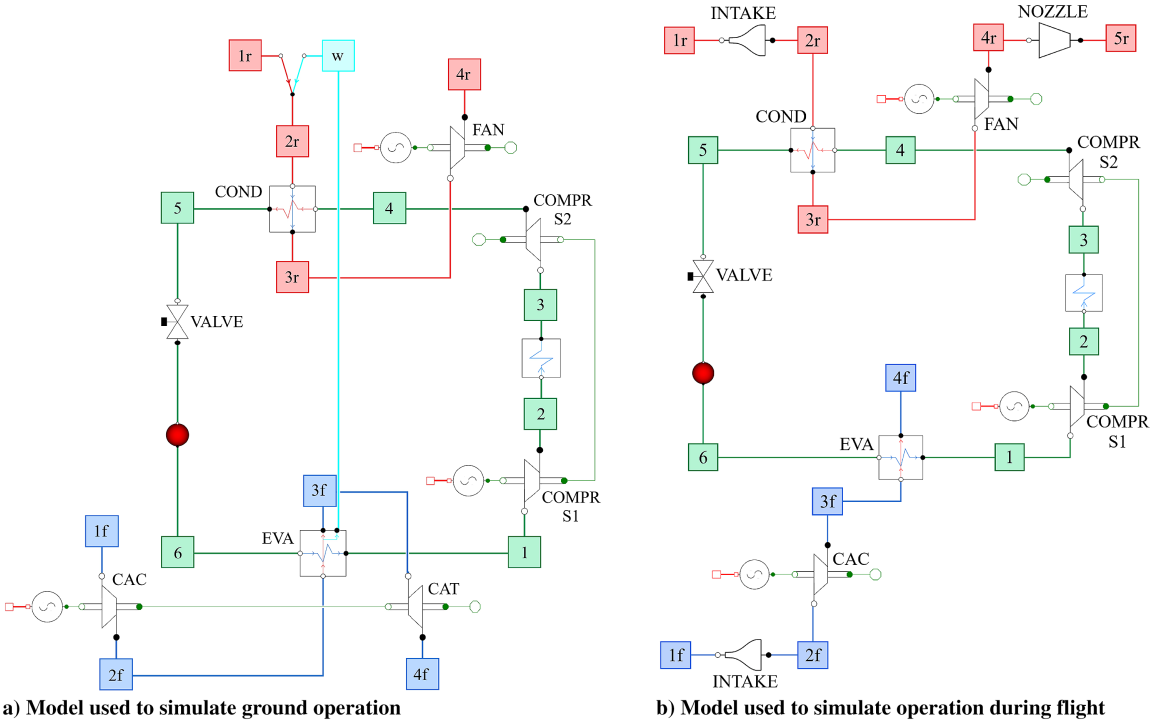

a) Model used to simulate ground operation b) Model used to simulate operation during flight

Fig. 2 Modelica models of the VCC system. The thermodynamic states of the ram air stream, cabin air stream, and refrigerant loop are highlighted in red, blue, and green, respectively.

for both design and off-design simulations. The only exception is the centrifugal compressor, which is modeled by means of TurboSim, i.e., an in-house Python software documented in [19,20]. The adoption of a different modeling paradigm for the centrifugal compressor is dictated by two reasons: i) the availability of an established and validated compressor model; ii) the reduced complexity of the system model implemented in Modelica and thus the increased robustness of the numerical solver. The graphical representation of the models used to simulate ground operation of the ACM and VCC systems is displayed in Figs. 1 and 2, respectively. The models used to evaluate the performance of the ECS during flight feature two main differences. First, they include a model of the air intake of the cabin air and ram air streams. Secondly, they do not require the dehumidification loop, due to the negligible water content in the ambient air at high altitudes.

The working fluid selected for the VCC system is the standard refrigerant used for helicopter applications, i.e., the R134a, a hydrofluorocarbon (HFC) with null ODP and a GWP[¶] equal to 1300. In view of the novel regulations for a progressive phase-out of HFCs by 2036 in developed countries [21], hydrofluoroolefins (HFOs) and hydrochlorofluoro-olefins (HCFOs) are identified as

[¶]The authors consider the index GWP_{100} as a measure of the environmental impact of a substance with respect to that of CO_2 over a time horizon of 100 years.

Downloaded by Technische Universiteit Delft on July 17, 2025 | http://arc.aiaa.org | DOI: 10.2514/1.C038093

Downloaded by Technische Universiteit Delft on July 17, 2025 | http://arc.aiaa.org | DOI: 10.2514/1.C038093

the next-generation refrigerants, thanks to their short atmospheric lifetime and thus GWP values lower than one [22]. However, the selection of the optimal working fluid will be addressed in a future study if the VCC system shows superior performance with respect to the state-of-the-art ACM technology.

B. Model of Air Intakes

Air intakes are used to supply the cabin with fresh air and to provide ram air to the heat exchangers of the ECS packs. The air intakes can be of two types: i) scoop inlets, i.e., emergent air intakes characterized by high total pressure recovery over a broad range of Mach numbers, at the expense of high drag; ii) flush inlets, i.e., submerged air intakes generating less drag and featuring lower total pressure recovery. As reported in [23], the minimization of the drag penalty is paramount for the optimal design of thermal management systems; therefore, flush inlets are usually preferred when the amount of total pressure recovery is not a stringent constraint. The selected air intakes for this study feature the same geometry as the ones installed on the Boeing 747, i.e., a rectangular entry and a NACA curved-divergent ramp.

The intakes are modeled according to the methodology documented in [24]. The main nondimensional parameters characterizing the geometry of the flush inlet are selected to maximize the pressure recovery, as suggested in [23]. In particular, an aspect ratio AR equal to 4 and a ramp angle α equal to 7° are set as optimal values. The intakes' cross section is defined by the maximum mass flow rate they should process. For ECS applications, this corresponds to the values computed for ground operation during a hot and humid day. The drag penalty associated with a flush intake can be expressed as

$$\mathrm{D_{fl}} = \dot{m}_\infty v_\infty \frac{C_{\mathrm{D,fl}}}{2} \tag{1}$$

where $\dot{m}_\infty$ is the ideal mass flow processed by the intake in freestream conditions

$$\dot{m}_\infty = \rho_\infty v_\infty A \tag{2}$$

and $C_{\mathrm{D,fl}}$ is the drag coefficient. This is expressed as the sum of the ram drag coefficient, the spillage drag coefficient, and a correction accounting for the increase of drag at values of mass flow rate close to the choking point of the intake:

$$C_{\mathrm{D,fl}} = 2k_{\mathrm{fl}} \frac{\dot{m}}{\dot{m}_\infty} + k_\alpha k_{\mathrm{m}} k_{\mathrm{sp,fl}} C'_{\mathrm{D}} + \Delta C_{\mathrm{D}} \tag{3}$$

The coefficients of Eq. (3) are evaluated with the semi-empirical correlation reported in [24].

In the same fashion, the pressure recovery factor of a flush intake, which reads

$$C_{P,\mathrm{fl}} = \frac{P_{\mathrm{t},1} - P_\infty}{P_{\mathrm{t},\infty} - P_\infty} \tag{4}$$

is estimated as the sum of different coefficients evaluated with the semi-empirical correlations documented in [24]:

$$C_{P,\mathrm{fl}} = C_{P,\mathrm{m}} + \Delta C_{P,\mathrm{mf}} + \Delta C_{P,\alpha} + \Delta C_{P,\mathrm{w}} \tag{5}$$

C. Air-to-Air Heat Exchanger Model

The topology selected for the primary and secondary heat exchangers of the bleedless three-wheel bootstrap ACM is that of plate-fin heat exchangers. In this device, the hot and cold streams flow according to an unmixed crossflow arrangement. The flow passages are formed by corrugated fins, featuring triangular or rectangular cross sections, sandwiched between parallel plates. The fins are attached to the plates by brazing, soldering, welding, or adhesive bonding. The shape and density of the fins can be selected to meet the design specifications in terms of compactness and pressure drops. In the present work, offset strip fins are prescribed on the hot and cold sides, as displayed in Fig. 3. The heat transfer coefficient of this type of fin is 1.5–4 times higher than that of plain fin geometries, at the expense of a larger friction factor.

The geometry of offset strip fins is characterized by their length l_{f}, height b, pitch p_{f}, and thickness t_{f}. These geometrical parameters can be conveniently converted into nondimensional numbers to simplify the development of empirical correlations derived from experimental data, as documented in [26]. The resulting nondimensional groups are the fin pitch-to-height ratio $\alpha = \mathrm{p_f}/b$, fin thickness-to-length ratio $\delta = \mathrm{t_f}/l_{\mathrm{f}}$, and fin thickness-to-pitch ratio $\gamma = t_{\mathrm{f}}/p_{\mathrm{f}}$. As a result, the vector of parameters characterizing the design of plate-fin heat exchangers featuring offset strip fins can be expressed as

$$\boldsymbol{X}_{\mathrm{hex}} = [x, y, z, \alpha_{\mathrm{hot}}, \alpha_{\mathrm{cold}}, \delta_{\mathrm{hot}}, \delta_{\mathrm{cold}}, \gamma_{\mathrm{hot}}, \gamma_{\mathrm{cold}}] \tag{6}$$

The heat transfer coefficient and the pressure drop occurring in the core of the plate-fin heat exchanger are computed as a function of the Colburn factor j and the friction factor f, as follows:

$$h_{\mathrm{conv}} = j \frac{c_{\mathrm{p}} G}{Pr^{2/3}} \tag{7}$$

$$\Delta P = f \frac{l_{\mathrm{core}}}{D_{\mathrm{hyd}}} \frac{\rho v^2}{2} \tag{8}$$

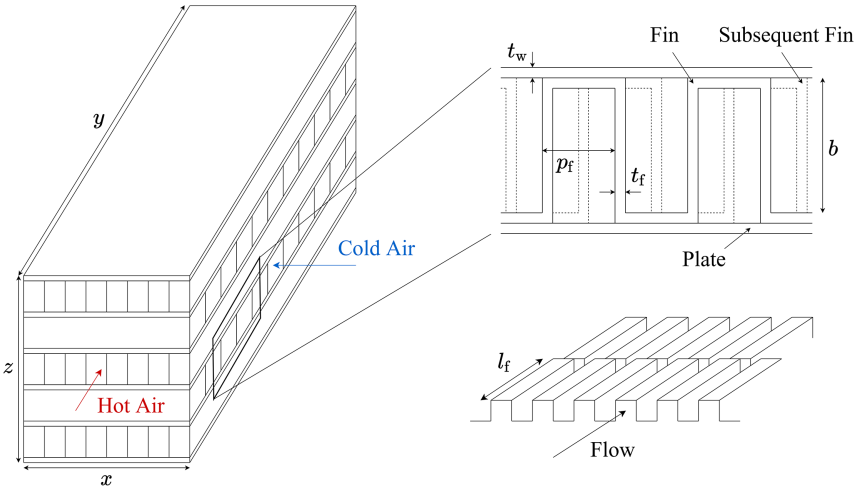

Fig. 3 Internal and external geometry of a plate-fin heat exchanger featuring offset strip fins.

In turn, j and f are estimated with the correlations documented in [27]. The heat transfer rate is computed with the ϵ-NTU method. The effectiveness ϵ can be interpreted as a thermal efficiency denoting the ratio between the actual heat transfer rate between the hot and cold fluids and the maximum possible heat transfer rate occurring in the ideal case. For an unmixed crossflow heat exchanger, it is expressed as

$$\epsilon = 1 - \exp\left\{\frac{\mathrm{NTU}^{0.22}}{C_\mathrm{r}}\left[\exp\left(-C_\mathrm{r}\mathrm{NTU}^{0.78}\right) - 1\right]\right\} \tag{9}$$

The thermal capacity ratio $C_\mathrm{r} = C_\mathrm{min}/C_\mathrm{max}$ is a dimensionless parameter defined as the ratio between the maximum and the minimum heat transfer capacity of the two media. The NTU is defined as the product of the overall heat transfer coefficient U and the total heat transfer surface A, divided by the minimum heat transfer capacity between the two working fluids.

$$\mathrm{NTU} = \frac{\mathrm{UA}}{C_\mathrm{min}} = \frac{1}{C_\mathrm{min}(R_\mathrm{th,hot} + R_\mathrm{th,w} + R_\mathrm{th,cold})} \tag{10}$$

where the thermal resistance of the plate is equal to

$$R_\mathrm{th,w} = \frac{\mathrm{t_w}}{\lambda_\mathrm{w} A_\mathrm{w}} \tag{11}$$

and that of the two media is expressed as

$$R_\mathrm{th} = \frac{1}{\eta h_\mathrm{conv} A} \tag{12}$$

Notably, η, h_conv, and A assume different values on the hot and cold sides. The efficiency of the extended surface is computed as

$$\eta = 1 - \left\{1 - \frac{\tanh\left[m(b/2 - t_\mathrm{f})\right]}{m(b/2 - t_\mathrm{f})}\right\}\frac{A_\mathrm{f}}{A_\mathrm{tot}} \tag{13}$$

where

$$m = \sqrt{2\frac{h_\mathrm{conv}}{\lambda_\mathrm{w} t_\mathrm{f}}\left(1 + \frac{t_\mathrm{f}}{l_\mathrm{f}}\right)} \tag{14}$$

and the ratio between the fin area and the total heat transfer surface is evaluated as reported in [25].

In addition to the friction through the heat exchanger core, the hot and cold streams experience pressure drops due to the sudden flow contraction and expansion occurring at the inlet and outlet of the flow passage. This effect is induced by the change in the free-flow area, as a result of the blockage introduced by the presence of the fins and plates. According to the methodology documented in [25], these pressure drops can be expressed as

$$\begin{aligned}\Delta P_\mathrm{in} &= \frac{(\dot{m}/A_\mathrm{ff})^2}{2\rho_\mathrm{in}}(1 - \sigma^2 + K_\mathrm{c})\\ \Delta P_\mathrm{out} &= \frac{(\dot{m}/A_\mathrm{ff})^2}{2\rho_\mathrm{out}}(1 - \sigma^2 - K_\mathrm{e})\end{aligned} \tag{15}$$

where σ represents the ratio between the minimum free-flow area and the frontal area, while K_c and K_e are the contraction and expansion coefficients, which are computed as a function of σ and the Reynolds number. The correlations used for the calculation of the heat transfer coefficient and the pressure drops have been verified using a case study documented in [28]. The results are reported in Table 1.

In design mode, the conditions at the inlet and outlet of the heat exchanger are known, but the geometry is not completely specified. For example, the model can be used to compute the height of the heat exchanger, which is equivalent to determining the number of flow passages, in order to meet the prescribed heat duty. Conversely, in off-design mode, the geometry of the heat exchanger is given, and the model is used to compute the heat transfer at the corresponding operating conditions. The dry weight of the heat exchanger is computed as the product of the density of the prescribed material and the total volume of the core, multiplied by an empirical coefficient to account for the presence of the casing, manifold, and soldering. The volume of the core is computed as the sum of the volume occupied by the fins V_f, and that of the plates V_p. With reference to Fig. 3, these can be expressed as

$$\begin{aligned}V_\mathrm{f} &= (b_\mathrm{hot} - t_\mathrm{f,hot} + p_\mathrm{f,hot})t_\mathrm{f,hot}N_\mathrm{f,hot}y\\ &\quad + (b_\mathrm{cold} - t_\mathrm{f,cold} + p_\mathrm{f,cold})t_\mathrm{f,cold}N_\mathrm{f,cold}x\\ V_\mathrm{p} &= \mathrm{t_w}xy(N_\mathrm{p} + 2) + b_\mathrm{hot}y\mathrm{t_w}(N_\mathrm{p} + 1) + b_\mathrm{cold}x t_\mathrm{w}N_\mathrm{p}\end{aligned} \tag{16}$$

Table 1 Comparison between the predictions of the heat transfer and pressure drop correlations adopted in the plate-fin heat exchanger model, and a case study reported in [28]

Working fluid	Property	Deviation
Air: hot side	Heat transfer coefficient	±0.9%
Air: cold side	Heat transfer coefficient	±7.1%
Air: hot side	Pressure drop	±2.9%
Air: cold side	Pressure drop	±0.3%

D. Air-to-Refrigerant Heat Exchanger Model

The two compact heat exchangers featured in the VCC system, i.e., the condenser and the evaporator, share the same topology. This consists of a stack of alternate flat tubes with internal microchannels and multilouvered fins brazed on the external surface. The air and the refrigerant flow according to an unmixed crossflow arrangement. In particular, the air flows through the passages created by the fins, where the boundary layer is continuously broken up, thus enhancing the heat transfer rate [29]. On the other side, the refrigerant undergoes a phase change along the microchannels, which are used to increase the heat transfer surface. With reference to Fig. 4, the vector of parameters characterizing the geometry of this type of heat exchanger reads

$$\begin{aligned}\boldsymbol{X}_\mathrm{hex} = [&x, y, z, b, F_\mathrm{p}, F_\mathrm{d}, l_\mathrm{f}, l_\mathrm{t}, L_\mathrm{h}, L_l, L_\mathrm{p}, N_\mathrm{mc}, N_\mathrm{f}, N_\mathrm{t},\\ &T_\mathrm{h}, \delta_\mathrm{f}, \delta_\mathrm{t}, \delta_\mathrm{mc}, \Theta]\end{aligned} \tag{17}$$

To correctly estimate the variation of fluid properties along the channel where phase change occurs, the model is divided into a number of control volumes corresponding to the number of working fluid phases, i.e., liquid, saturated fluid, and vapor. As an example, the condenser is thus divided into three sections: desuperheating (superheated vapor), condensing (liquid-vapor in thermodynamic equilibrium), and subcooling (subcooled liquid). This modeling approach is known as moving boundary (MB) method. Pangborn et al. [30] demonstrated that the MB method enables a better tradeoff between model complexity and accuracy as compared to the traditional finite volume method. The length of each control volume is computed as a function of the phase of the refrigerant and the corresponding enthalpy change. An average thermodynamic state is defined in each control volume, by assuming a linear distribution of enthalpy and pressure between the inlet and outlet boundaries. The remaining flow properties, e.g., density, are retrieved from the average thermodynamic state by using the multiparameter equation of state implemented in REFPROP [31]. The MB approach allows for the selection of the most proper correlations to compute the heat transfer coefficient and the pressure drop within the HEXs according to the refrigerant phase. These empirical correlations are based on nondimensional numbers, i.e., the Colburn factor j and the Nusselt number Nu for the heat transfer coefficient, and the friction factor f for the pressure drop. A detailed list of the set of equations selected for the evaporator and the condenser models is provided by Ascione et al. [17].

Downloaded by Technische Universiteit Delft on July 17, 2025 | http://arc.aiaa.org | DOI: 10.2514/1.C038093

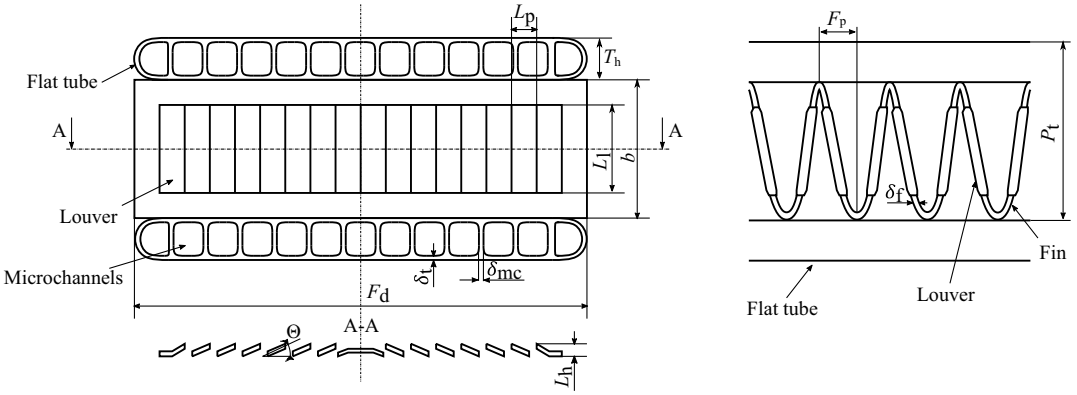

Fig. 4 Schematic of the multilouvered fins and flat tubes heat exchanger geometry [17].

Analogously to the plate-fin heat exchanger model, the ϵ-NTU method has been used to estimate the heat transfer rate. The effectiveness is computed as indicated in Eq. (9) for single-phase flow. In the case of evaporation or condensation of the fluid within the heat exchanger tubes, the heat capacity ratio C_r is equal to zero, and therefore the effectiveness is defined as

$$\epsilon = 1 - e^{-\mathrm{NTU}} \tag{18}$$

The thermal conductance UA used in the expression of the NTU is computed by accounting for the effect of convection and of conduction through fins and tubes

$$\mathrm{NTU} = \frac{\mathrm{UA}}{C_{\min}} = \frac{1}{C_{\min}(R_{\mathrm{th,air}} + R_{\mathrm{th,refr}} + R_{\mathrm{th,wall}})} \tag{19}$$

The thermal resistance of the air $R_{\mathrm{th,air}}$ is determined as in Eq. (12), where the heat transfer coefficient of air is estimated using the correlation proposed by Chang and Wang [32]. The thermal resistance of the refrigerant flow $R_{\mathrm{th,refr}}$ is inversely proportional to the heat transfer coefficient of the refrigerant stream multiplied by the surface available for the heat transfer. The heat transfer coefficient of the refrigerant stream is calculated using the correlation developed by Kandlikar [33] in the case of evaporating flow, and the one assessed by Shah [34] in the case of condensation. Following the methodology presented by [35], the thermal resistance of the microchannel walls is estimated as

$$R_{\mathrm{th,t}} = \frac{1}{2\pi\lambda}\left(\frac{1}{l_t N_{\mathrm{mc}} N_t}\right)\log\left(\frac{T_h}{T_h - 2\delta_{\mathrm{mc}}}\right) \tag{20}$$

Analogously to the heat transfer coefficient, different correlations are employed to estimate the pressure loss due to friction depending on the fluid phase and the geometry of the heat exchanger. The empirical relation proposed by Kim et al. [36] is chosen to estimate the friction coefficient f of the airflow through the passages formed by the multilouvered fins. In the case of single-phase refrigerant flow, the pressure drop is estimated using a well-assessed set of equations specific to horizontal straight tubes, which depend on the flow regime [37]. The model by Schmidt and Friedel [38] is adopted to retrieve the friction coefficient of two-phase refrigerant flow. Once the tube geometry and the fluid mass flow rate are selected, and the inlet and outlet effects associated with flow contraction and expansion are neglected, the overall pressure drop is retrieved as

$$\Delta P = f\frac{l_t}{D_{\mathrm{hyd}}}\frac{\rho v^2}{2} \tag{21}$$

The experimental data by Kim et al. [39] have been used for the validation of the condenser model. In particular, the results indicate a deviation of 10% in the pressure drop calculation and a discrepancy of 4% in the heat transfer surface estimation. This validation can also be applied to the evaporator, as both heat exchangers share the same topology. It was not possible to perform a validation of the heat transfer coefficient due to the lack of experimental data. However, all the correlations implemented in the heat exchanger models have been verified with experimental data available in the open literature, and the results of this analysis can be found in the work by Giuffré et al. [16].

Similarly to the model of the air-to-air plate fin heat exchanger (Sec. II.C), the condenser and evaporator models can be used for both design and off-design simulations. In design mode, the model computes the width of the air-side cross section, corresponding to the microchannels length. This modeling approach is different from the one chosen for the air-to-air heat exchanger design, in which the unknown geometrical variable is the height of the HEX. This modeling choice is driven by the different physical mechanisms governing the heat transfer in the two devices. In the air-to-air heat exchanger, the same working fluid is used on both sides, and no phase change occurs. Therefore, any of the three dimensions characterizing the volume of the HEX can be selected as a free variable in design mode. The height has been chosen as a free variable in this work, as it determines the number of identical flow passages that are required to comply with the design point heat flow rate. In the case of the condenser and evaporator, however, the refrigerant flowing within the passages formed by the microchannels undergoes a phase change. Therefore, the length of the tubes is the most natural choice of free geometrical variable in design mode. With reference to Fig. 4, for weight estimation purposes, the volume occupied by the fins, V_f, and that of the microchannel tubes, V_t, can be expressed as

$$V_f = \delta_f[(b^2 + F_p^2)^{1/2} - \delta_f]F_d N_f$$
$$V_t = x\left[\frac{\pi}{2}\delta_t N_t(T_h + F_d - 2\delta_t) + \delta_{\mathrm{mc}}(T_h - 2\delta_t)(N_{\mathrm{mc}} - 1)\right] \tag{22}$$

The weight of the two-phase heat exchanger is computed in the same fashion as for the air-to-air heat exchanger.

E. Centrifugal Compressor Model

The cabin air compressor (CAC) and the refrigerant compressor (RC) are the critical turbomachinery components of the two ECS configurations considered in this study. The CAC is the main consumer of electric power, whereas the design of the RC affects the operating range and COP of the VCC system. The methodology used to model single-stage and twin-stage centrifugal compressors is thoroughly described in [19,20], respectively, and is not treated in this section for conciseness.

With reference to Fig. 5, the conceptual design of a centrifugal compressor stage is uniquely defined by eight design variables, namely, the swallowing capacity $\phi_{t1} = \dot{m}/\rho_{t1}U_2D_2^2$; the isentropic work coefficient $\psi_{is} = \Delta h_{tt,is}/U_2^2$; the impeller shape factor $k = 1 - (R_{1,\mathrm{hub}}/R_{1,\mathrm{shroud}})^2$; the absolute flow angle at impeller outlet, α_2; the number of blades, N_{bl}; the diffuser radius ratio R_3/R_2; and the nondimensional parameters characterizing the shape of the

Downloaded by Technische Universiteit Delft on July 17, 2025 | http://arc.aiaa.org | DOI: 10.2514/1.C038093

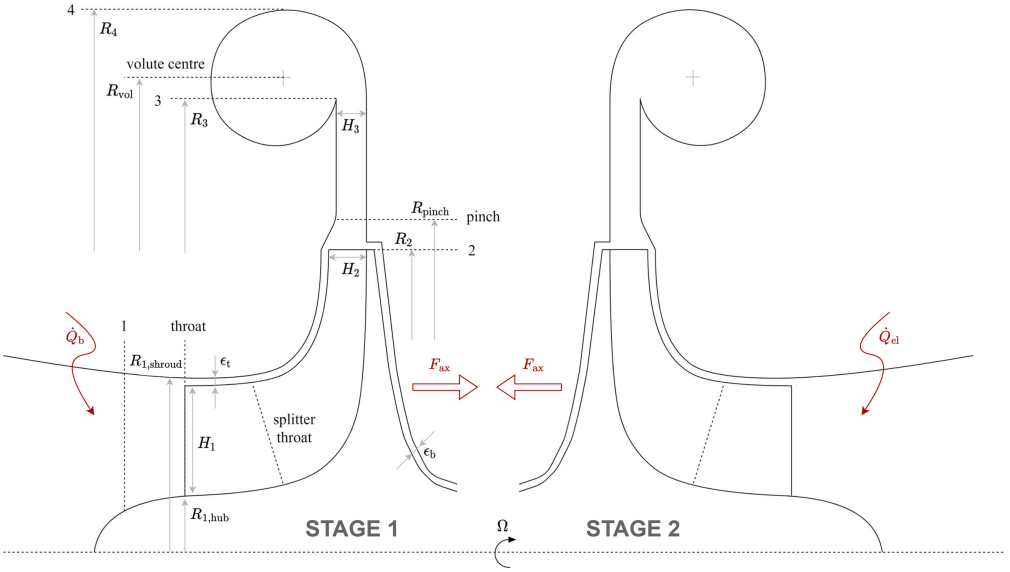

Fig. 5 Schematic view of a twin-stage centrifugal compressor on the meridional plane [20].

diffuser, $R_{r,pinch} = (R_{pinch} - R_2)/(R_3 - R_2)$ and $H_{r,pinch} = (H_3 - H_2)/(H_2(R_2/R_{pinch} - 1))$. Furthermore, the model requires the specification of the working fluid, nominal pressure ratio β_{tt}, nominal mass flow rate $\dot{m}$, total inlet conditions, and a list of geometrical parameters related to manufacturing, e.g., the impeller tip clearance gap.

Moreover, the value of the intermediate pressure must be specified in a twin-stage compressor configuration if it is not constrained by the design of the VCC system. As documented in [20], this can be expressed as a function of the splitting factor κ_s:

$$\begin{cases} \beta_{tt}|_{s1} = \kappa_s \sqrt{\beta_{tt}/\kappa_s} \\ \beta_{tt}|_{s2} = \sqrt{\beta_{tt}/\kappa_s} \end{cases} \tag{23}$$

In turn, the vector of parameters characterizing the design of a twin-stage centrifugal compressor reads

$$\boldsymbol{X}_{comp} = [\beta_{tt}, \dot{m}, \kappa_s, \phi_{t1}|_{s1-s2}, \psi_{is}|_{s1}, \alpha_2|_{s1-s2}, k|_{s1-s2}, N_{bl}|_{s1-s2}, R_3/R_2|_{s1-s2}, R_{r,pinch}|_{s1-s2}, H_{r,pinch}|_{s1-s2}] \tag{24}$$

The two impellers of a twin-stage compressor are mounted in a back-to-back configuration (see Fig. 5) such that the net axial thrust is minimized and can be balanced by gas bearings, which cannot sustain high axial loads. In this work, the axial thrust is computed following the approach devised by Tiainen et al. [40]. Furthermore, the cooling of the electric motor must be properly modeled, as it can significantly affect the performance of the machine. In the configuration adopted in this work, the flow at the outlet of the first stage is used to cool the motor before entering the second stage. The resulting compressor assembly is very compact and does not rely on external cooling flows for thermal management. As a drawback, the refrigerant vapor is heated in between the two compressor stages, causing a fluid dynamic efficiency penalty in the order of five percentage points.

TurboSim can be used for both design and off-design simulations. Moreover, it has been validated with the experimental data of three reference test cases available in the literature [41–46], and with CFD data. The in-house tool is complemented with a method for preliminary weight estimation, accounting for the weight of the compressor assembly and electric motor. The former is computed via a parametric CAD model automatically generated by resorting to CadQuery [47]. The latter is estimated based on the predicted values of power density for high-speed permanent magnet synchronous machines, according to the method documented in [48]. The correlations implemented in the model of the electric motor are derived by assuming liquid jacket cooling and are valid for rotor surface speeds up to 200 m/s and electrical power ratings as high as 1 MW. The rotor outer radius, used to compute the surface speed, is set to match the maximum mechanical power required by the compressor, after accounting for the electrical efficiency and the windage losses. The electrical efficiency is estimated by means of the values reported in [48], while the windage loss is computed according to the method documented in [49].

F. Integrated Design Optimization

The design optimization problem involves three objectives: the minimization of the electric power consumption, weight, and drag penalty associated with the two ECS packs. For the bleedless ACM architecture, the weight of each pack is calculated as the sum of the weight of the CAC and that of the primary and secondary HEXs. In the first approximation, the weight of the three-wheel ACM and that of the dehumidification loop are omitted from the calculation of the objective function due to the absence of reliable models. Nevertheless, the weight of the three-wheel ACM is negligible as compared to that of the CAC due to the sizeable difference in power rating and the absence of an electric motor. In the same fashion, the weight of the condenser and reheater is negligible as compared to that of the primary and secondary HEXs due to the substantial difference in heat flow rate processed by such components. In the case of the VCC system, the weight of each pack accounts for the contributions of the CAC, RC, evaporator, condenser, and working fluid charge. The working fluid charge is computed considering the amount circulating in the system during steady-state operation plus an additional quantity used to ensure safe startup of the VCC system. The material considered for the heat exchangers of the ACM and the VCC system is the aluminum alloy 3003, whereas the CAC and the RC are assumed to be made of the aluminum alloy 2219-T852.

The optimization targets three operating conditions of the ECS: standard cruise conditions, ground operation on a hot and humid day, and flying operation in case of a faulty pack. The ECS thermal load

Table 2 Specifications of the operating points selected for the multipoint design optimization

Variable	Hot ground	Cruise	Faulty pack
T_{amb}, K	311.15	216.65	216.65
P_{amb}, kPa	101.32	19.68	19.68
Φ_{amb}, %	22	0	0
$\dot{m}_{pack}$, kg/s	0.5	0.5	0.88
T_{pack}, K	256.95	276.55	273.69
P_{pack}, kPa	102.4	76.27	76.25

Downloaded by Technische Universiteit Delft on July 17, 2025 | http://arc.aiaa.org | DOI: 10.2514/1.C038093

Downloaded by Technische Universiteit Delft on July 17, 2025 | http://arc.aiaa.org | DOI: 10.2514/1.C038093

associated with such operating points has been computed by means of a thermal model of the pressurized aircraft compartments, developed in-house and validated with proprietary data provided by Airbus [50]. The results are reported in Table 2. The main components of the system, namely, the heat exchangers and the centrifugal compressors, are sized for the case of hot ground conditions, i.e., the operating point characterized by the highest heat load. Then, their off-design performance is evaluated for cruise and faulty pack operation. Similarly, the air intakes are sized to accommodate the maximum mass flow rate, obtained in faulty pack conditions, and their off-design performance is evaluated in cruise conditions. The values of electric power consumption and drag penalty included in the objective function are computed as a weighted average.

$$\overline{P_{\text{el}}} = 0.3P_{\text{el,hg}} + 0.6P_{\text{el,cr}} + 0.1P_{\text{el,fp}} \tag{25}$$

$$\bar{D} = 0.8D_{\text{cr}} + 0.2D_{\text{fp}} \tag{26}$$

In Eqs. (25) and (26), the electric power consumption and the drag penalty must be doubled at ground and cruise conditions to account for the simultaneous operation of two ECS packs. Moreover, the choice of the weights assigned to each operating point is arbitrary and directly affects the result of the optimization. Consequently, more relevance has been given to the performance metrics computed at cruise conditions, followed by those obtained during hot ground operation. Conversely, the power consumption and the drag penalty computed for the faulty pack case have a limited influence on the objective functions since the performance of the ECS should not be optimal in such conditions. Nevertheless, to ensure the required level of redundancy for certification purposes, each optimal solution needs to meet the prescribed set point in faulty pack conditions. The vector of objective functions reads

$$\boldsymbol{J} = [\overline{P_{\text{el}}}, W, \bar{D}] \tag{27}$$

The flowchart of the new multi-objective and multipoint optimization framework, hereinafter referred to as Design Optimization of Energy Conversion Systems (DesOptECS), is displayed in Fig. 6. It consists of a Python program coupling the ECS models developed in Modelica, the compressor model implemented in Python, and an open-source toolbox for multi-objective design optimization [51]. With reference to Fig. 6, the vector $\boldsymbol{\alpha}$ includes the variables related to the design of the system, heat exchangers, and compressors:

$$\boldsymbol{\alpha} = [\boldsymbol{\alpha}_{\text{sys}}, \boldsymbol{\alpha}_{\text{hex}}, \boldsymbol{\alpha}_{\text{comp}}] \tag{28}$$

Some of the parameters characterizing the design of the compressors and heat exchangers can be set to fixed values to reduce the size of the optimization problem and therefore to expedite the calculation. As a result, $\boldsymbol{\alpha}_{\text{hex}}$ and $\boldsymbol{\alpha}_{\text{comp}}$ may include fewer elements than $\boldsymbol{X}_{\text{hex}}$ and $\boldsymbol{X}_{\text{comp}}$; see Eq. (6), Eq. (17), and Eq. (24). For example, when performing the optimization of the VCC system, only the y and z dimensions of the condenser and evaporator core have been included in the vector $\boldsymbol{\alpha}_{\text{hex}}$, whereas the parameters characterizing the design of the fins and microchannels have been set to constant values, since they have only a secondary influence on the values of the objective functions. The design variables and the corresponding upper and lower bounds prescribed for the optimization of the two ECS configurations are reported in Tables A1 and A2 of Appendix A. The total number of design variables pertaining to the ACM and VCC optimization is equal to 25 and 27, respectively.

Two sets of nonlinear constraints have been prescribed for the design optimization of the two ECS configurations. In particular, the constraints are set to ensure the manufacturability of the system components, i.e., heat exchangers and compressors, and to define an upper threshold for the speed of the air and the refrigerant in the circuit, as well as for the corresponding pressure drops. Overall, the design optimization of the ACM and the VCC system features 17 and 41 nonlinear constraints, as summarized in Tables A1 and A2 of Appendix A, respectively.

The optimization algorithm used in this study is the NSGA-II [52], i.e., a well-established evolutionary algorithm suited for multi-objective constrained optimization problems. The initial population comprises 10 individuals for each design variable. The corresponding

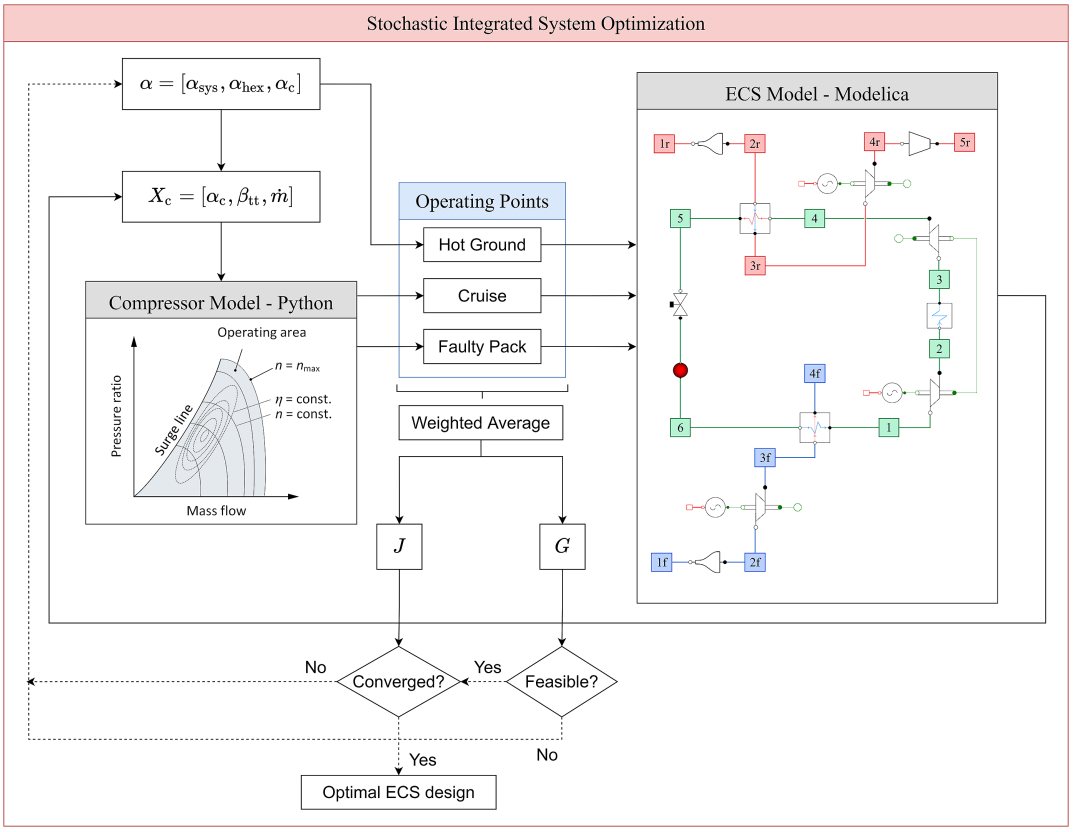

Fig. 6 Flowchart of the multi-objective and multipoint optimization framework DesOptECS.

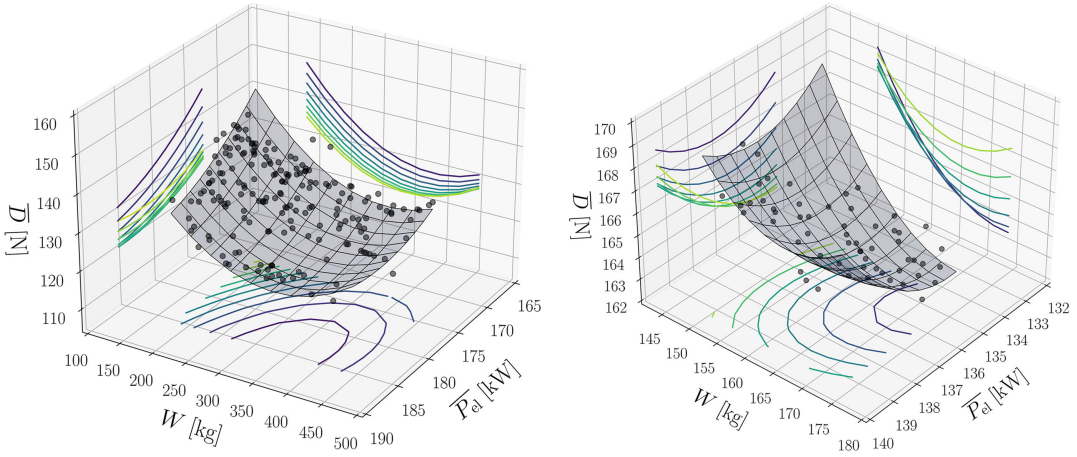

a) Bleedless ACM b) Electrically-driven VCC system

Fig. 7 Three-dimensional Pareto front computed for the two candidate ECS architectures.

Downloaded by Technische Universiteit Delft on July 17, 2025 | http://arc.aiaa.org | DOI: 10.2514/1.C038093

design space is sampled according to the Latin hypercube methodology. The optimization algorithm met the convergence criterion after 139 and 112 generations for the ACM and the VCC system, respectively, leading to a total number of 34,750 and 30,240 evaluations of the Modelica models for each operating point. The optimizations have been performed on an Intel Xeon Gold 5220R processor featuring a clock speed up to 4.0 GHz. The resulting computational cost is approximately equal to 1056 core-hours for the ACM and 2880 core-hours for the VCC system. The discrepancy in the computational cost required by the two optimization problems is due to the higher complexity of the VCC system model, involving the evaluation of three compressor stages with TurboSim and the use of a multiparameter equation of state to model the thermodynamic behavior of R134a.

III. Results

The three-dimensional Pareto fronts identified by the optimization algorithm for the two candidate ECS configurations are displayed in Fig. 7. To facilitate the quantitative comparison between the performance metrics of the two systems, the same results are illustrated on the power-weight, power-drag, and weight-drag planes in Fig. 8. Moreover, the optimal design point leading to the minimum fuel weight penalty W_{f0} is highlighted with a red marker. The fuel weight penalty associated with the ECS is computed as the sum of three contributions [53]:

1) Penalty due to additional weight:

$$W_{f0} = W\left[\exp\left(\frac{SFC_{th}\tau}{L/D}\right) - 1\right] \tag{29}$$

2) Penalty associated with shaft power off-take:

$$W_{f0} = P_{el}SFC_P\frac{L/D}{SFC_{th}}\left[\exp\left(\frac{SFC_{th}\tau}{L/D}\right) - 1\right] \tag{30}$$

3) Penalty associated with additional drag:

$$W_{f0} = D\frac{L/D}{g}\left[\exp\left(\frac{\mathrm{SFC}_{th}\tau}{L/D}\right) - 1\right] \tag{31}$$

The values of the parameters in Eqs. (29–31) depend on the aircraft type, engine specifications, and prescribed flight phase. In this work, the required set of aircraft parameters is representative of an Airbus A320 [1], i.e., thrust-specific fuel consumption $SFC_{th} = 0.514$ lb/(lbf · h), power-specific fuel consumption $SFC_P = 0.5$ lb/(hp · h), lift-to-drag ratio $L/D = 15.32$, and mission time $\tau = 1.5$ h.

By comparing the Pareto fronts associated with the optimal designs of the bleedless ACM and the VCC system, it is possible to observe that the VCC system is characterized by lower weight and lower electric power consumption but features a higher drag penalty. In particular, by selecting the design points leading to the minimum fuel weight penalty for the two ECS architectures, the weight saving is $W \approx 40$ kg, the power saving is $\overline{P_{el}} \approx 41$ kW, and the additional drag penalty is $\bar{D} \approx 28$ N. As a result, the fuel weight penalty associated with the optimal VCC system configuration is approximately 18% lower than the one of the optimal bleedless ACM. This is a conservative estimate since the three-wheel ACM as well as the reheater and condenser are not accounted for in the weight computation.

To gain further insights, it is possible to analyze the influence of each objective function on the value of the fuel weight penalty, as displayed in Fig. 9. The fuel weight penalty of the bleedless ACM features a linear dependency with the weight and an inverse proportionality with the drag. These trends are mainly affected by the design of the primary and secondary heat exchangers. A more compact design of the heat exchangers leads to lower weight and higher pressure drops. The increase in the pressure drops leads to a higher drag penalty, but also to a higher power consumption of the CAC to meet the pressure set point at the pack discharge. However, as one can notice in Fig. 9, the design points associated with lower drag or lower electric power consumption feature a remarkable increase in the system weight. In turn, the higher weight offsets any potential reduction in fuel consumption due to lower drag and lower electric power consumption, leading to a suboptimal design. As a result, the optimal design of the bleedless ACM corresponds to the one characterized by the minimum weight.

The design of the evaporator and the condenser of the VCC system is affected by the same tradeoff between compactness and pressure drops that characterizes the design of the air-to-air heat exchangers of the ACM. However, in the case of the VCC system, the combined weight of the two heat exchangers is comparable to the sum of the weights of the CAC and the RC. Therefore, the minimization of the weight and the drag penalty of the VCC system can be partially decoupled. The electric power consumption of the VCC system is affected by both the CAC and the RC. An increase in the pressure ratio of the RC leads to a rise of the temperature lift**, and ultimately to a higher temperature difference in the condenser. On the one hand, this allows the use of a more compact and lighter condenser, featuring a lower heat transfer surface. On the other hand, it leads to higher electric power consumption.

A. Air Cycle Machine

The design of the primary and secondary HEXs mainly affects the tradeoff between the weight and the drag penalty associated with the bleedless ACM architecture. The following analysis is focused on

**Evaluated as the difference between the condensation and the evaporation temperature of the refrigerant in the vapor compression cycle.

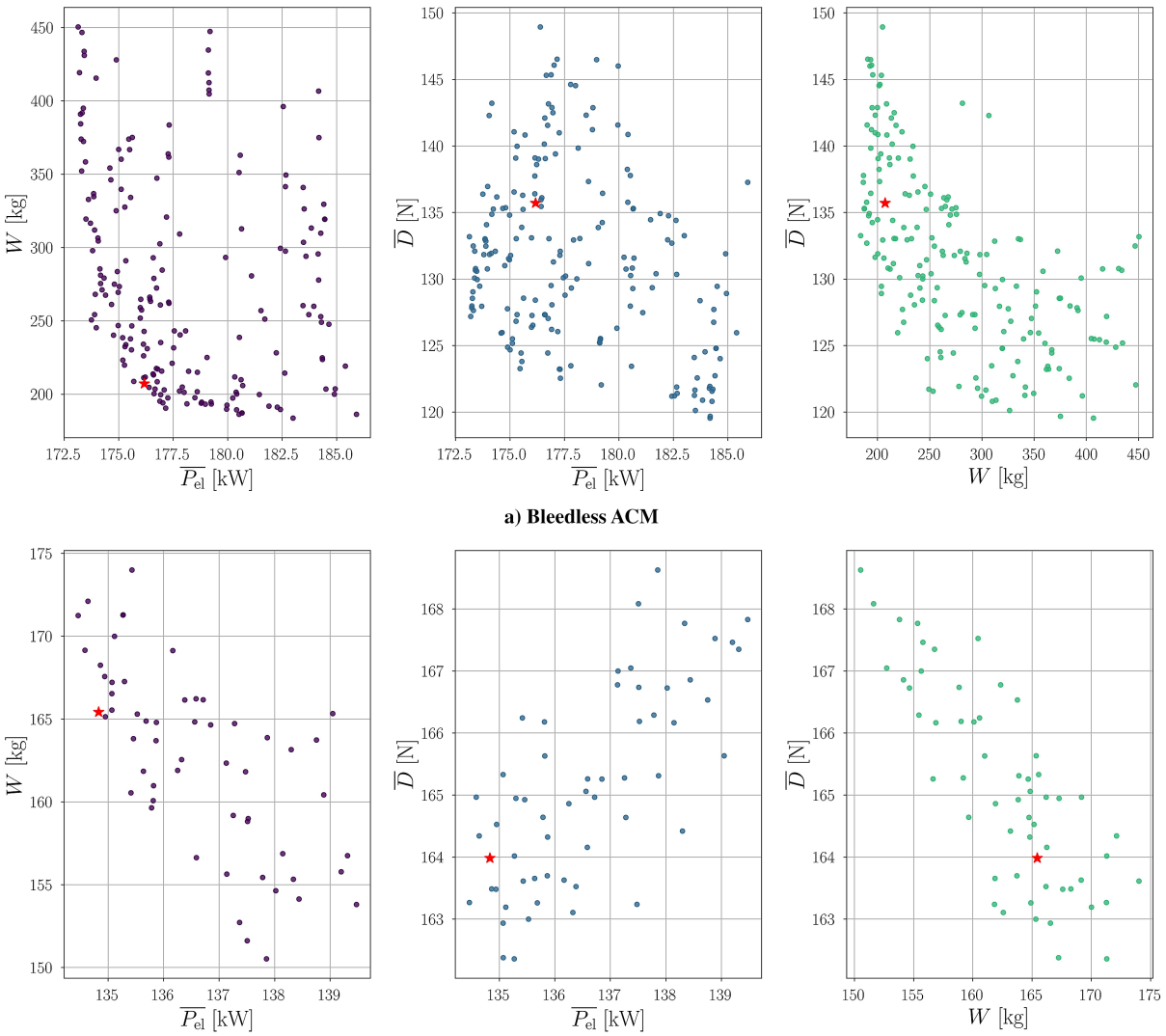

Fig. 8 Three-dimensional Pareto front projected on two-dimensional planes. The red marker identifies the design point leading to the minimum fuel weight penalty.

the secondary HEX, i.e., the one characterized by the highest heat load in the optimal ACM configuration. However, the considerations reported below are applicable also to the design of the primary heat exchanger. The influence of the dimensions of the secondary HEX core on its weight is displayed in Fig. 10. The weight primarily scales with the core height z_{hex_2}, which defines the number of flow passages. As a result, designs featuring large values of width and depth, i.e., x_{hex_2} ranging from 0.7 to 0.85 m and y_{hex_2} ranging from 0.75 and 0.9 m, are optimal as they lead to a lower height, i.e., $z_{\text{hex}_2} \approx 0.2$ m, thus lower weight. However, a lower height implies a smaller frontal area, leading to higher pressure drops. To illustrate this issue, Fig. 11 shows the variation of the pressure drop with the frontal area of the secondary HEX on the ram air side. As displayed in the chart, a reduction in the frontal area below the value associated with the design featuring the minimum fuel weight penalty produces an exponential increase in the pressure drop on the ram air side, thus in the drag penalty. The associated reduction in weight is not sufficient to compensate for the increase in drag, leading to a suboptimal design.

The variable that mostly affects the design and the performance of the CAC is the swallowing capacity $\Phi_{\text{t1,cac}}$, followed by the isentropic work coefficient $\psi_{\text{is,cac}}$. Figure 12 shows the influence of the swallowing capacity on the weight, average rotational speed, and average efficiency evaluated at the prescribed operating points. A higher value of $\Phi_{\text{t1,cac}}$ leads to higher rotational speed and efficiency. Moreover, compressor designs featuring higher rotational speed are more compact and lightweight, leading to an inverse proportionality between $\Phi_{\text{t1,cac}}$ and W_{cac}. This is in accordance with the design guidelines documented in [19]. However, the maximum value of $\Phi_{\text{t1,cac}}$ has been limited to 0.1 in this study, since higher values lead to diminishing returns in terms of efficiency and negatively affect the compressor operating range.

The relations between the compressor performance metrics and $\psi_{\text{is,cac}}$ are more complicated and require further explanation. The isentropic work coefficient measures the share of the work performed by the flow deflection within the impeller blade passage with respect to the contribution of the centrifugal potential $U_2^2/2$. A compressor featuring a higher value of $\psi_{\text{is,cac}}$ is characterized by higher blade loading and lower peripheral speed, thus lower rotational speed. However, the rotational speed is mostly affected by the value of the swallowing capacity. An increase in blade loading is usually associated with higher fluid-dynamic losses and lower compressor efficiency. Moreover, a higher blade loading implies a higher flow deflection, thus a higher impeller blade turning. This may lead to an unfeasible design of the impeller, characterized by forward-swept blades at the outlet. Conversely, the work coefficient cannot be arbitrarily reduced, since the impeller peripheral speed must be kept below a threshold, e.g., 600 m/s, to avoid structural issues, and the backsweep at the impeller outlet cannot exceed 45–50° to ensure manufacturability.

Downloaded by Technische Universiteit Delft on July 17, 2025 | http://arc.aiaa.org | DOI: 10.2514/1.C038093

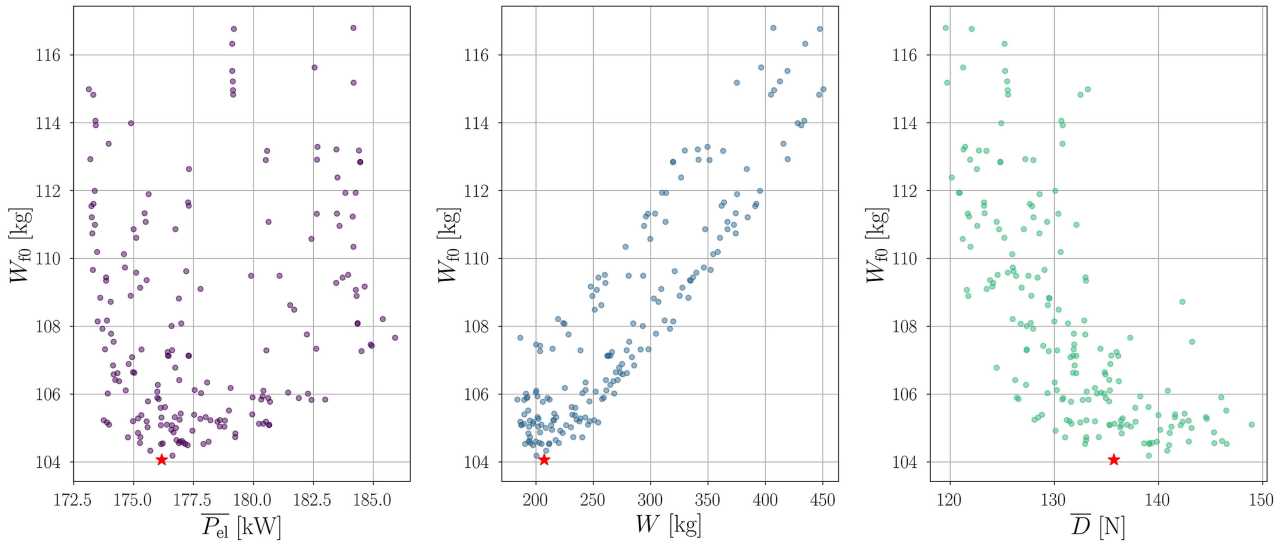

a) ECS based on the bleedless ACM architecture

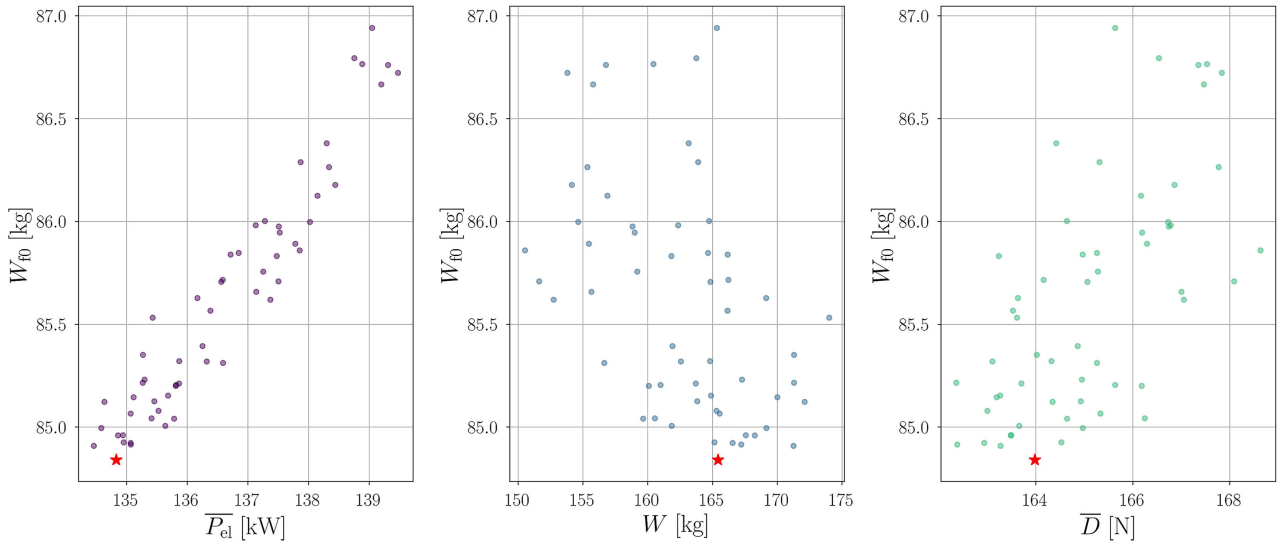

b) ECS based on the electrically-driven VCC system

Fig. 9 Fuel weight penalty vs objectives functions. The red marker identifies the design point leading to the minimum fuel weight penalty.

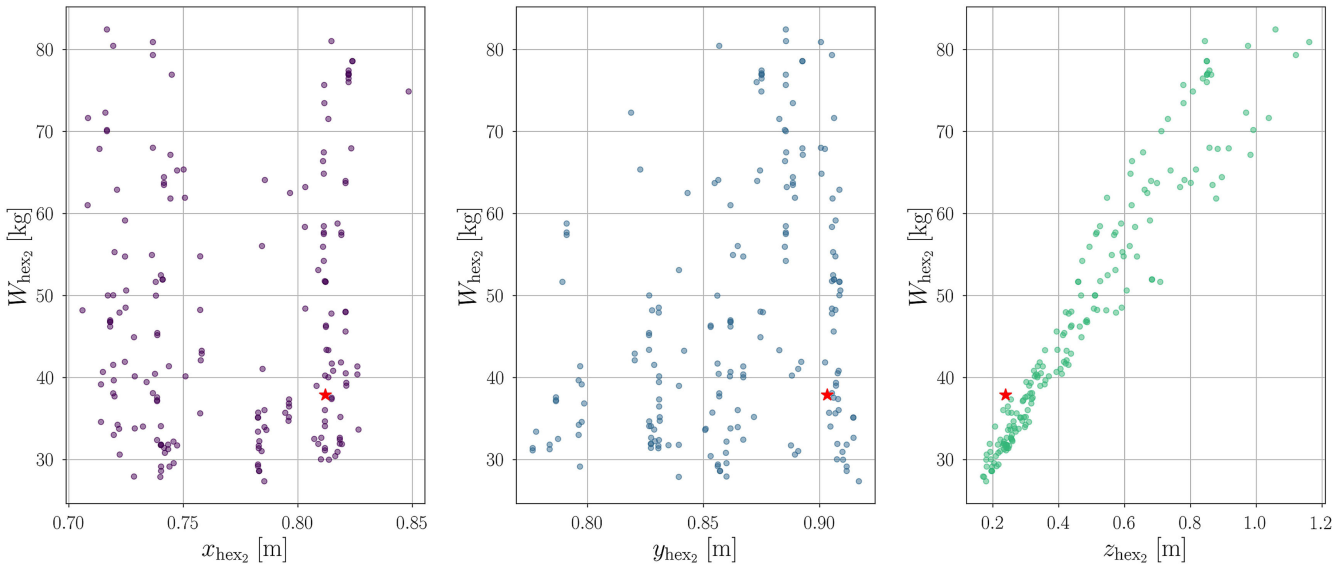

Fig. 10 Weight of secondary HEX vs core dimensions. The red marker identifies the design point leading to the minimum fuel weight penalty.

Downloaded by Technische Universiteit Delft on July 17, 2025 | http://arc.aiaa.org | DOI: 10.2514/1.C038093

Downloaded by Technische Universiteit Delft on July 17, 2025 | http://arc.aiaa.org | DOI: 10.2514/1.C038093

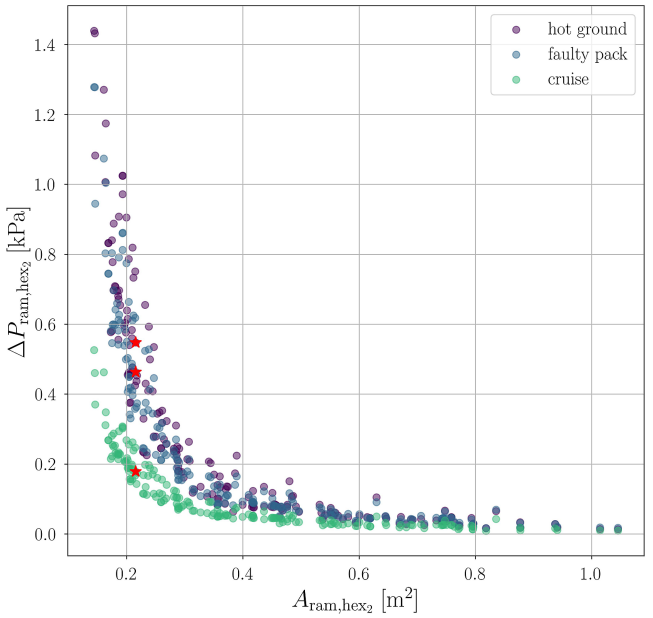

Fig. 11 Pressure drop on the ram air side of the ACM secondary HEX vs frontal area. The red marker identifies the design point leading to the minimum fuel weight penalty.

The set of design variables and nonlinear constraints characterizing the ACM layout leading to the minimum fuel weight penalty is reported in Table A1. Moreover, the corresponding temperature–entropy diagrams for ground and cruise operations are displayed in Fig. 13. Inspection of the thermodynamic diagrams shows that during ground operation the total heat load is split between the primary and secondary heat exchangers, with the secondary heat exchanger featuring a slightly higher duty, i.e., $\dot{Q}_{\mathrm{hex_1}} = 44.9$ kW and $\dot{Q}_{\mathrm{hex_2}} = 52.6$ kW. As a result, the two heat exchangers are characterized by a similar design, but the secondary HEX features larger core dimensions. Conversely, when the aircraft is at cruise conditions and the total heat load of the ECS pack is lower, the secondary HEX is responsible for most of the heat transfer, i.e., $\dot{Q}_{\mathrm{hex_1}} = 6.1$ kW and $\dot{Q}_{\mathrm{hex_2}} = 69.1$ kW. This is due to the small temperature difference between the fresh and ram air streams established in the primary HEX at cruise (see states 3-4 and 4r-5r in Fig. 13b). In such operating conditions, the primary HEX could be bypassed, and the cabin air could be cooled only with the secondary HEX. As a result, the drag penalty associated with the pressure drops on the ram air side could be further reduced. However, this would require substantial modifications of the ram air duct and therefore is not considered in the present study.

B. Vapor Compression Cycle System

The VCC system features two heat exchangers, i.e., the evaporator and the condenser. The design of the evaporator affects the tradeoff between the weight of the system and the electric power consumption of the CAC. Conversely, the tradeoff between the weight and the drag penalty is influenced by the design of the condenser.

The weight sensitivity of the evaporator with respect to its core dimensions is displayed in Fig. 14. The weight scales linearly with the width of the evaporator, which defines the length of the microchannels. Most of the optimal designs populating the Pareto front feature approximately the same value of evaporator height ($y_{\mathrm{eva}} \approx 0.5$ m) and depth ($z_{\mathrm{eva}} \approx 0.1$ m). Moreover, the Pareto front is complemented by a group of optimal designs characterized by a higher value of the height ($y_{\mathrm{eva}} \approx 0.75$ m). Within this cluster of design points, the linear proportionality between the evaporator weight and width is characterized by a higher slope, as displayed in the left chart of Fig. 14. The lack of optimal solutions between the two groups featuring $y_{\mathrm{eva}} \approx 0.5$ m and $y_{\mathrm{eva}} \approx 0.75$ m can be explained by investigating the dependence of the evaporator characteristics on the core height. For this purpose, a test case has been set up. The set of variables characterizing the design of the VCC system has been prescribed according to the solution leading to the minimum fuel weight penalty. Moreover, the evaporator depth has been set to $z_{\mathrm{eva}} = 0.1$ m, and the height has been linearly varied in the range $y_{\mathrm{eva}} = 0.5$–1 m. The resulting values of the evaporator width and weight are shown in Fig. 15a; the corresponding pressure drops computed for the air and the refrigerant sides are displayed in Fig. 15b. Given a fixed heat load, the higher the evaporator height, the lower the corresponding width. However, in this case, the decrease of x_{eva} does not compensate for the increase of y_{eva}, leading to a higher evaporator weight and a higher frontal area on the air and refrigerant sides. In turn, this yields a reduction of the pressure drops on both sides, which ultimately reduces the electric power consumption of the CAC and RC. In light of these considerations, the existence of two groups of optimal y_{eva} values can be interpreted as follows. To minimize the weight of the VCC system, it is necessary to design a compact and lightweight evaporator, which can be achieved by selecting $y_{\mathrm{eva}} \approx 0.5$ m. Conversely, if the primary objective is to minimize the electric power consumption, the designer should select a higher value of evaporator height in order to minimize pressure drops. Intermediate values of the

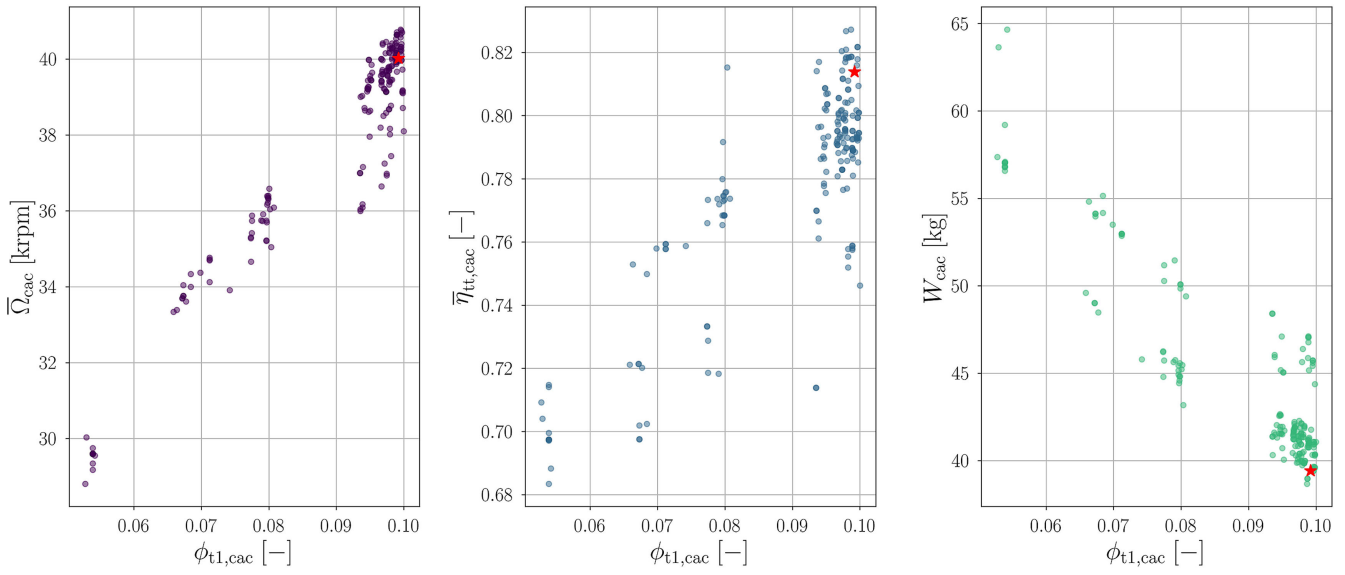

Fig. 12 Influence of the swallowing capacity on the main performance metrics of the CAC. The red marker identifies the design point leading to the minimum fuel weight penalty.

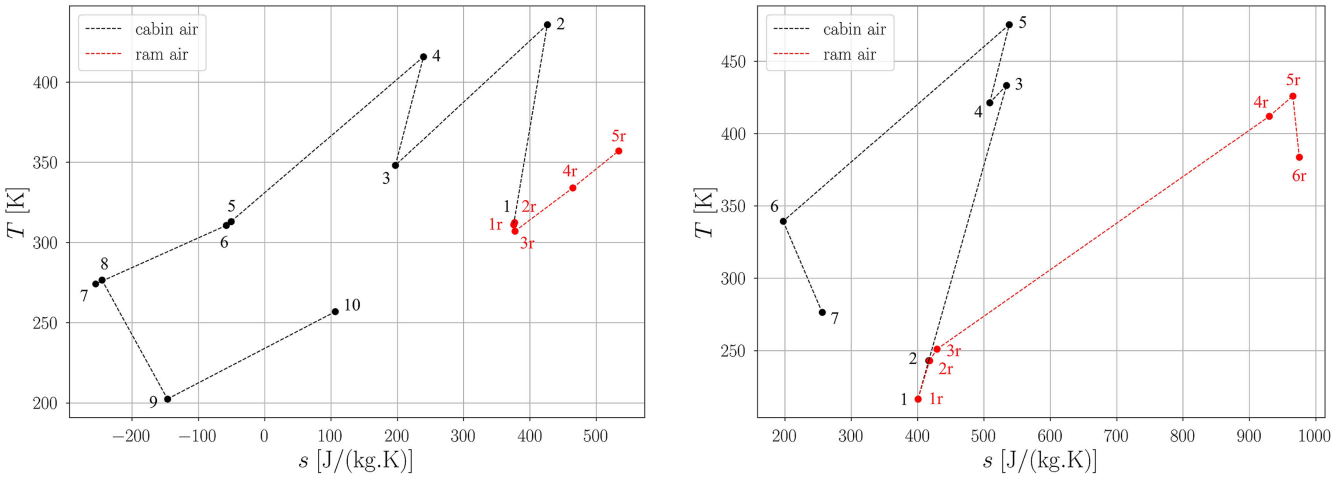

a) Hot ground operation b) Cruise operation

Fig. 13 Temperature–entropy diagrams of the optimal bleedless ACM architecture. The thermodynamic states are numbered with reference to the system schematic displayed in Fig. 1.

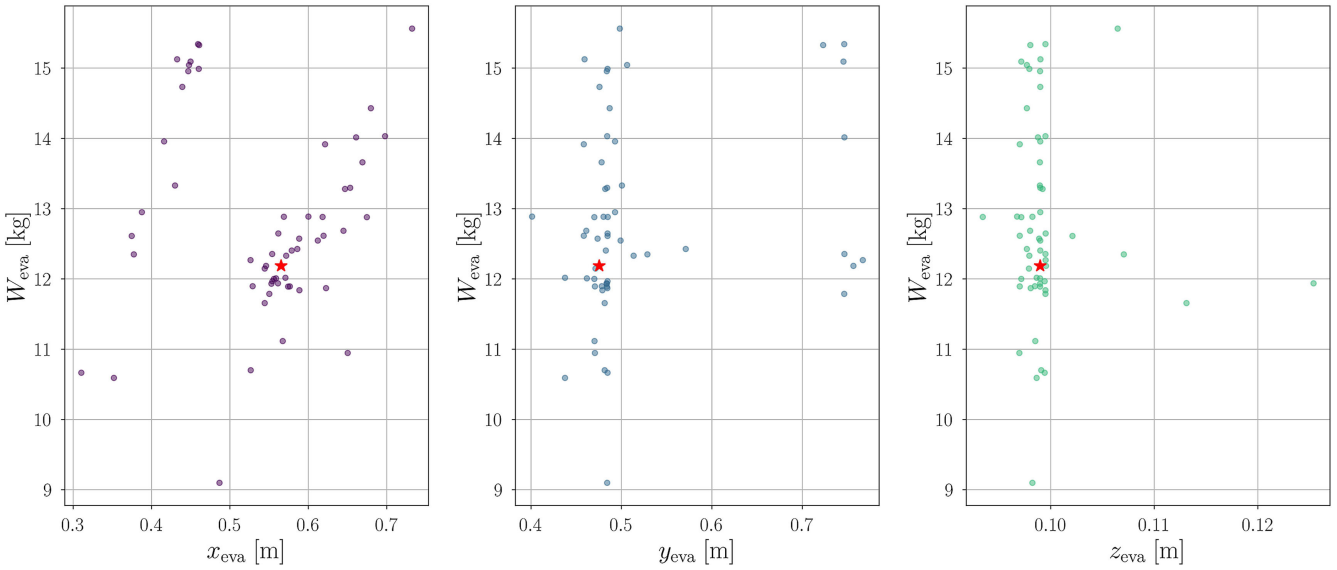

Fig. 14 Weight of evaporator vs core dimensions. The red marker identifies the design point leading to the minimum fuel weight penalty.

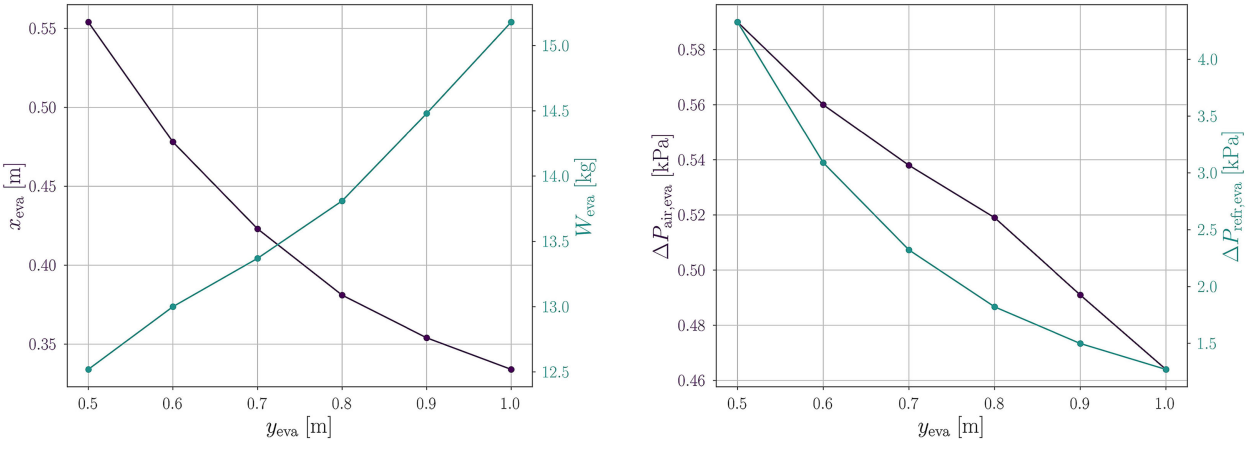

a) Evaporator width and weight b) Pressure drop on ram air and refrigerant sides

Fig. 15 Influence of core height on evaporator design and performance.

evaporator height lead to feasible but suboptimal solutions and thus are discarded by the optimizer.

The dependence of the condenser pressure drop on the ram air side on its frontal area is displayed in Fig. 16a. Moreover, the variation of the pressure drops on the refrigerant side as a function of the condenser width is shown in Fig. 16b. As expected, the air-side pressure drop is inversely proportional to the frontal area, while the refrigerant side pressure drop is linearly dependent on the length of the micro-

Downloaded by Technische Universiteit Delft on July 17, 2025 | http://arc.aiaa.org | DOI: 10.2514/1.C038093

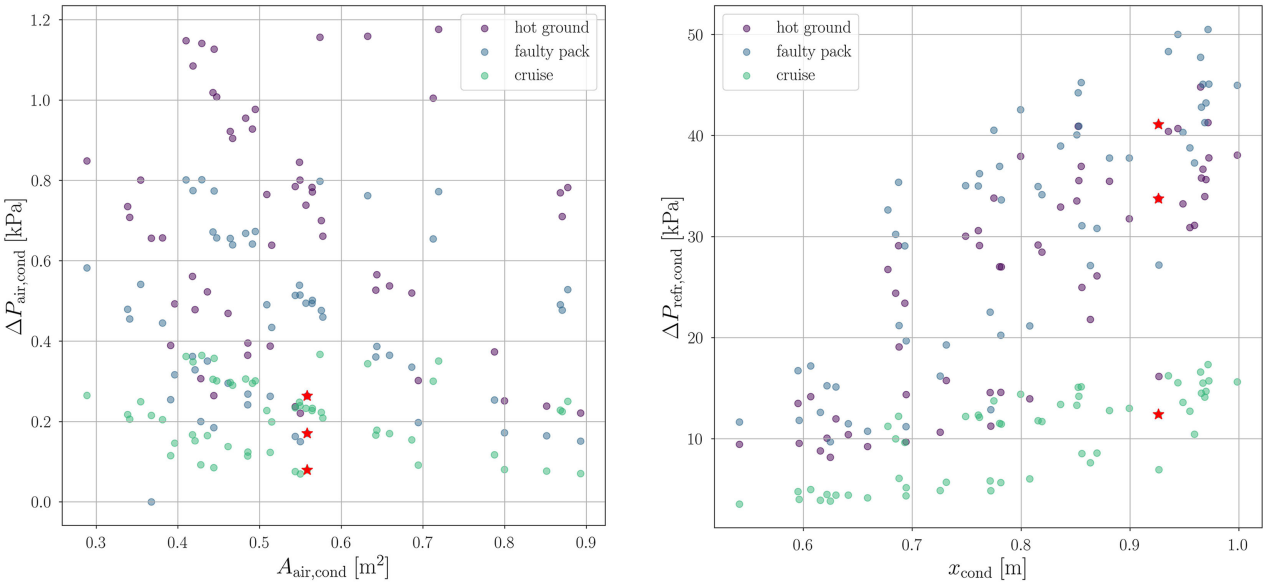

a) Ram air side **b) Refrigerant side**

Fig. 16 Condenser pressure drop vs frontal area and width. The red marker identifies the design point leading to the minimum fuel weight penalty.

channels, i.e., the condenser width. The red markers highlight how optimal designs are obtained by prioritizing the minimization of the air-side pressure drop at the expense of a higher pressure drop along the refrigerant side. This is in accordance with the results reported in Fig. 9b, which shows that the optimal VCC design point lies in the design space associated with the lowest drag penalty.

In the VCC system, the only function of the CAC is to provide the required pressurization of the cabin air. Thus, the CAC is characterized by a lower pressure ratio than in the case of the bleedless ACM architecture. This allows the selection of a higher value of swallowing capacity, in accordance with the design guidelines reported in [19]. The resulting design therefore features lower rotational speed, lower weight, and, on average, higher efficiency than the CAC of the bleedless ACM.

The two variables that mostly affect the design and performance of the twin-stage RC are the ratio between the swallowing capacity of the two stages and the pressure ratio splitting factor. The values selected by the optimizer are shown in Fig. 17, together with the resulting compressor speed and efficiency averaged over the three prescribed points selected for the multipoint optimization. By inspecting the left chart of Fig. 17, one can notice that all the optimal design points are characterized by $\kappa_s > 1$ and $\phi_{t1}|_{s1}/\phi_{t1}|_{s2} > 2$. In other words, all the optimal RC design points feature a higher pressure ratio in the first stage and a value of swallowing capacity of the first stage that is at least double that of the second stage. These results are in line with the design guidelines for twin-stage compressors documented in [20]. In a nutshell, the selection of a higher swallowing capacity and pressure ratio in the first stage allows us to obtain similar values of the isentropic loading coefficient for the two stages, thus leading to optimal compressor efficiency. Moreover, the operating range of the twin-stage compressor is typically limited by the stability margins of the second stage. As documented in [19], the design space associated with maximum operating range for a centrifugal compressor stage lies at lower values of swallowing capacity than the locus of optimal efficiency. Therefore, the selection of a lower value of $\phi_{t1}|_{s2}$ enables a higher operating range of the second stage, thus of the entire twin-stage compressor. Overall, the optimal RC design is characterized by a moderate rotational speed $\bar{\Omega} \approx 100$ krpm and by an average total-to-total efficiency in excess of 74%, accounting for the losses introduced by the cooling of the electric motor.

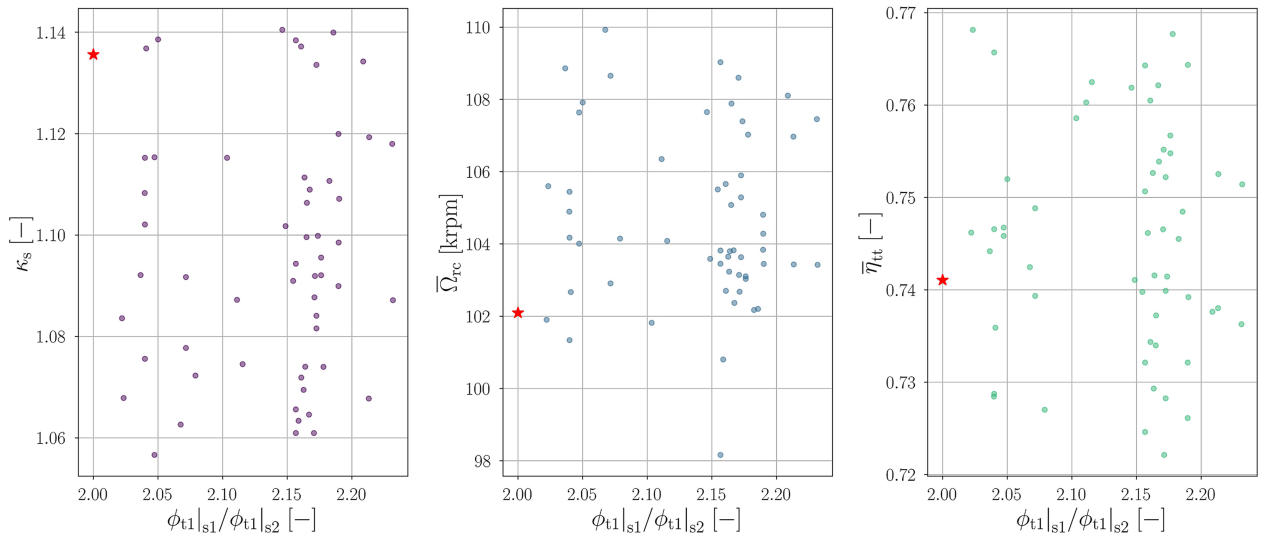

Fig. 17 Influence of the swallowing capacity ratio on the main performance metrics of the twin-stage RC. The red marker identifies the design point leading to the minimum fuel weight penalty.

Downloaded by Technische Universiteit Delft on July 17, 2025 | http://arc.aiaa.org | DOI: 10.2514/1.C038093

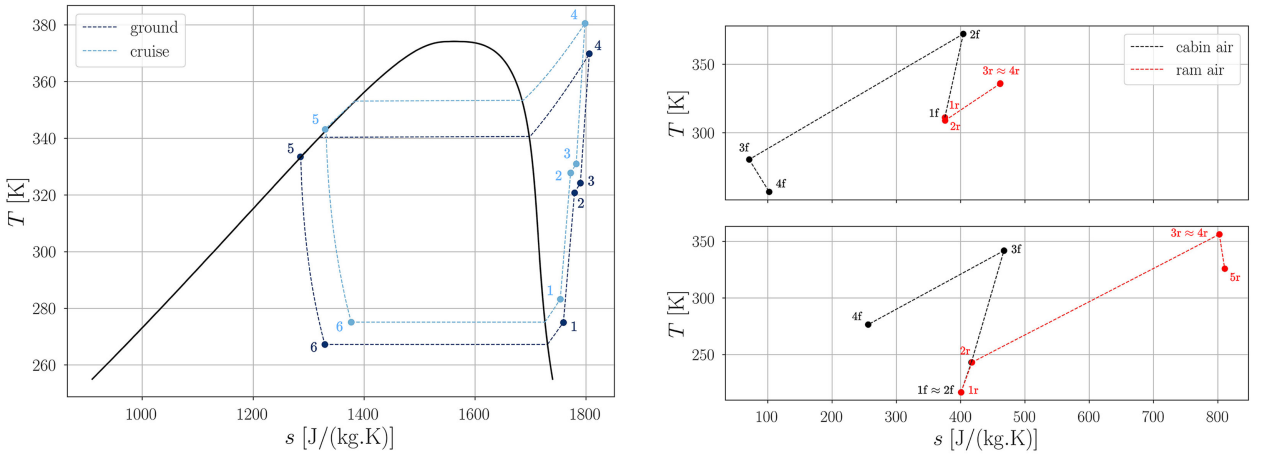

a) Refrigerant loop operating with R134a

b) Ram and cabin air streams

Fig. 18 Temperature–entropy diagrams of the optimal VCC system operating at hot ground and cruise conditions. The thermodynamic states are numbered with reference to process flow diagram of Fig. 2.

Downloaded by Technische Universiteit Delft on July 17, 2025 | http://arc.aiaa.org | DOI: 10.2514/1.C038093

The set of design variables and constraints characterizing the optimal VCC system configuration is reported in Table A2. The associated temperature–entropy diagrams evaluated at ground and cruise conditions are displayed in Fig. 18. The heat load of the condenser and the evaporator is approximately 37% higher on the ground than in cruise conditions, and this is primarily due to a 30% increase in the mass flow rate of refrigerant in ground conditions. This effect, combined with the large variation of the environmental conditions between the two operating points, leads to a sizeable increase in the ram air mass flow rate, i.e., from $\dot{m}_{\text{ram}}|_{\text{cr}} = 0.47$ kg/s to $\dot{m}_{\text{ram}}|_{\text{hg}} = 3.02$ kg/s. As a result, the minimization of the condenser air-side pressure drop is of paramount importance not only to reduce the drag penalty but also to limit the power consumption of the ram air fan during ground operation. Conversely, the variation of the evaporation and condensation temperatures between the two operating points is limited to 7.8°C and 12.8°C, respectively. As a consequence, the change in the temperature lift and the pressure ratio provided by the RC is only minor. This is due to the presence of the cabin air turbine downstream of the evaporator, which enables cooling of the cabin air below 0°C during ground operation, without significantly altering the evaporation temperature.

IV. Conclusions

A novel integrated design method for aircraft ECS has been developed and documented in this work. The methodology encompasses a multipoint and multi-objective optimization strategy that simultaneously accounts for the preliminary design of the system and its main components. The models of the ECS components have been implemented in the in-house Modelica library DeSimECS. The only exception is the centrifugal compressor, whose design and operating map are computed with the in-house model TurboSim described in [19,20]. The integrated design framework has been used to optimize and compare the simulated performance of two different ECS configurations: a bleedless three-wheel bootstrap ACM and an electrically driven VCC system. The vehicle under analysis is a single-aisle, short-haul aircraft, e.g., the Airbus A320, and the prescribed operating points are hot ground, cruise, and high-altitude flight in the presence of a faulty ECS pack. The main outcomes of this study can be summarized as follows:

1) The optimal ECS configuration based on the electrically driven VCC system, featuring compact heat exchangers and high-speed centrifugal compressors, is both lighter ($\Delta W \approx 40$ kg) and more energy-efficient ($\Delta \overline{P_{\text{el}}} \approx 41$ kW) than the state-of-the-art bleedless ACM architecture. However, if compared to the most compact ACM design, the VCC system causes a higher drag penalty ($\Delta \bar{D} \approx 28$ N). Overall, the fuel weight penalty computed for the optimal VCC system is approximately 18% lower than the one evaluated for the optimal bleedless ACM.

2) The optimal design point of the VCC system lies in the region of minimum electric power consumption. Conversely, the minimization of the fuel weight penalty related to the bleedless ACM is primarily driven by the minimization of the system weight.

3) The design of the primary and secondary heat exchangers of the ACM is dictated by the tradeoff between weight and pressure drop, which directly affects the drag penalty. For both the heat exchangers, the design leading to the minimum fuel weight penalty is characterized by similar width and depth and a lower height. At the sizing condition, i.e., hot ground operation, the heat load is split between the two HEXs, with the secondary HEX featuring a slightly higher duty, thus larger dimensions. At cruise conditions, the whole thermal heat load could be theoretically processed by the secondary HEX, while the primary HEX could be bypassed to reduce the drag penalty generated by the pressure drop on the ram air side.

4) The design of the evaporator affects the tradeoff between the weight and the electric power consumption of the VCC system. Conversely, the design of the condenser determines the tradeoff between the weight and the drag penalty. For both heat exchangers, the minimization of the pressure drop on the ram air side is more beneficial than the reduction of the refrigerant-side pressure drop. As a result, the optimal design features a large frontal area on the air side, long microchannels, and a short airflow path.

5) The optimal design of the twin-stage RC of the VCC system is in line with the design guidelines reported in [20]. In particular, the first stage is characterized by a value of swallowing capacity that is more than double that of the second stage, whereas the isentropic work coefficient has similar values for the two stages. Moreover, the first stage is always characterized by a higher pressure ratio than the second stage. For the prescribed ECS operating points, the mass flow rate of refrigerant is approximately 60% higher during faulty pack operation than at cruise conditions, whereas the variation of the pressure ratio of the two stages is minor. This leads to stringent requirements on the operating range of the machine, therefore highlighting the need for a multipoint optimization strategy to obtain a feasible design.

The results of this research reveal the importance of adopting an integrated design approach when pursuing the optimization of complex energy conversion systems, such as the ECS of passenger aircraft. Moreover, the results of this work, although only numerical, prove the potential of an electrically driven VCC system, featuring compact heat exchangers and high-speed centrifugal compressors. Therefore, this technology is envisaged to replace partly or completely bleedless ACM systems in next-generation aircraft. Future work will investigate the performance of more complex VCC system architectures, featuring multiple pressure levels, and will include the selection of the working fluid as an additional degree of freedom of the integrated design optimization. The optimization framework could be further extended to enable the use of mixtures by including

the mixture composition as an additional design variable. However, in the case of zeotropic mixtures, this would entail a modification of the heat exchanger models to account for the nonlinear distribution of the enthalpy in each control volume [54]. Moreover, it would require the implementation of heat transfer coefficient correlations specifically developed for zeotropic mixtures [55,56].

Appendix

The design variables and the nonlinear constraints prescribed for the integrated design optimization of the three-wheel bleedless ACM and the electrically driven VCC are reported in Tables A1 and A2, respectively. The optimal design values correspond to the design point associated with the minimum fuel weight penalty.

Table A1 Design variables and nonlinear constraints used for the integrated design optimization of the three-wheel bleedless air cycle machine

Design variable	Category	Range	Optimal value
$T_r\|_{hg}$	System - hot ground	0.45–0.65	0.49
$\dot{m}_{ram}\|_{hg}$, kg/s	System - hot ground	1.6–2.0	1.91
$\beta_{tt}\|_{cac,cr}$	System - cruise	3.5–4.5	3.54
$\beta_{tt}\|_{cac,fp}$	System - faulty pack	5.0–5.5	5.05
$\phi_{t1}\|_{cac}$	Compressor	0.05–0.1	0.01
$\psi_{is}\|_{cac}$	Compressor	0.65–0.85	0.66
$\alpha_2\|_{cac}$, deg	Compressor	60–70	66
$R_3\|_{cac}/R_2\|_{cac}$	Compressor	1.3–1.8	1.3
k_{cac}	Compressor	0.75–0.95	0.86
$x_{hex_1-hex_2}$, m	Heat exchanger	0.6–1.1	0.6–0.81
$y_{hex_1-hex_2}$, m	Heat exchanger	0.6–1.1	0.65–0.9
$\alpha_{hot}\|_{hex_1-hex_2}$	Heat exchanger	0.1–1	0.45–0.29
$\delta_{hot}\|_{hex_1-hex_2}$	Heat exchanger	0.01–0.05	0.017–0.016
$\gamma_{hot}\|_{hex_1-hex_2}$	Heat exchanger	0.01–0.15	0.047–0.068
$\alpha_{cold}\|_{hex_1-hex_2}$	Heat exchanger	0.1–1	0.21–0.43
$\delta_{cold}\|_{hex_1-hex_2}$	Heat exchanger	0.01–0.05	0.024–0.018
$\gamma_{cold}\|_{hex_1-hex_2}$	Heat exchanger	0.01–0.15	0.019–0.016
Constraint	**Category**	**Threshold**	**Max/min value**
$\max(P_m\|_{fan})$, kW	System	10	3.44
$\min(R_{1,hub}\|_{cac})$, mm	Compressor	3.25	29.2
$\min(H_2\|_{cac})$, mm	Compressor	1.4	12.1
$\min(\beta_{2,bl}\|_{cac})$, deg	Compressor	−50	−49.7
$\max(\beta_{2,bl}\|_{cac})$, deg	Compressor	−10	−49.7
$\max(M_3\|_{cac})$	Compressor	0.7	0.61
$\min(\Omega\|_{cac})$, krpm	Compressor	30	36.63
$\max(\Omega\|_{cac})$, krpm	Compressor	250	42.54
$\max(U_2\|_{cac})$, m/s	Compressor	600	482.5
$\min(z_{hex_1-hex_2})$, m	Heat exchanger	0.05	0.34–0.24
$\max(z_{hex_1-hex_2})$, m	Heat exchanger	1.2	0.34–0.24
$\max(v_{hot}\|_{hex_1-hex_2})$, m/s	Heat exchanger	50	16.2
$\max(v_{cold}\|_{hex_1-hex_2})$, m/s	Heat exchanger	50	17.0

The set of optimal values corresponds to the ACM design leading to the minimum fuel weight penalty. With reference to Fig. 1a, $T_r = (T2 - T3)/(T2 - T10)$.

Table A2 Design variables and nonlinear constraints used for the integrated design optimization of the electrically driven vapor compression cycle system

Design variable	Category	Range	Optimal value
$\Delta T_{sh}\|_{hg}$, K	System - hot ground	3–10	8.55
$\Delta T_{sc}\|_{hg}$, K	System - hot ground	3–10	9.82
$\Delta T_{sh}\|_{cr}$, K	System - cruise	3–10	8.39
$\Delta T_{sc}\|_{cr}$, K	System - cruise	3–10	9.95
$\Delta T_{sh}\|_{fp}$, K	System - faulty pack	3–10	9.66
$\Delta T_{sc}\|_{fp}$, K	System - faulty pack	3–10	9.29
$\dot{m}_{ram}\|_{hg}$, kg/s	System - hot ground	2.8–3.5	3.02
$T_{eva}\|_{hg}$, K	System - hot ground	253.15–268.15	267.30
$\beta_{tt}\|_{cac,hg}$	System - hot ground	1.5–2	1.70
$\beta_{tt}\|_{s1,hg}$	System - hot ground	2.9–3.3	3.22
$\beta_{tt}\|_{s2,hg}$	System - hot ground	2.7–3.1	2.74
$\beta_{tt}\|_{s1,cr}$	System - cruise	2.7–3.1	3.01

Downloaded by Technische Universiteit Delft on July 17, 2025 | http://arc.aiaa.org | DOI: 10.2514/1.C038093

Table A2 (*Continued.*)

Design variable	Category	Range	Optimal value
$\beta_{tt}\|_{s2,cr}$	System - cruise	2.5–2.9	2.83
$\beta_{tt}\|_{s1,fp}$	System - faulty pack	2.7–3.1	3.06
$\beta_{tt}\|_{s2,fp}$	System - faulty pack	2.5–2.9	2.62
$\phi_{t1}\|_{cac}$	Compressor	0.08–0.15	0.15
$\phi_{t1}\|_{s1}$	Compressor	0.1–0.18	0.16
$\phi_{t1}\|_{s2}$	Compressor	0.04–0.1	0.08
$\psi_{is}\|_{cac}$	Compressor	0.75–0.9	0.76
$\psi_{is}\|_{s1}$	Compressor	0.65–0.85	0.82
$\alpha_2\|_{cac-s1-s2}$, deg	Compressor	60–70	69.5–69.2–67.1
y_{eva}, m	Heat exchanger	0.3–1	0.48
y_{cond}, m	Heat exchanger	0.5–1.2	0.60
$z_{eva-cond}$, m	Heat exchanger	0.03–0.4	0.10–0.03
Constraint	**Category**	**Threshold**	**Max/min value**
$\max(P_m\|_{fan})$, kW	System	10	1.19
$\min(R_{1,hub}\|_{cac-s1-s2})$, mm	Compressor	3.25	26.50–3.37–4.15
$\min(H_2\|_{cac-s1})$, mm	Compressor	1.4	24.38–3.30
$\min(H_2\|_{s2})$, mm	Compressor	1.2	1.55
$\min(\beta_{2,bl}\|_{cac-s1-s2})$, deg	Compressor	10	38.79–28.10–23.40
$\max(\beta_{2,bl}\|_{cac-s1-s2})$, deg	Compressor	50	38.79–28.10–23.40
$\max(M_3\|_{cac-s1-s2})$	Compressor	0.7	0.41–0.64–0.66
$\min(\Omega\|_{cac})$, krpm	Compressor	10	20.41
$\min(\Omega\|_{s1-s2})$, krpm	Compressor	30	100.28
$\max(\Omega\|_{cac-s1-s2})$, krpm	Compressor	250	27.70–103.06
$\max(U_2\|_{cac-s1-s2})$, m/s	Compressor	600	310.58–206.19–193.37
$\max(\Delta F_{ax}\|_{s1-s2})$, N	Compressor	400	367.9
$\min(x_{eva-cond})$, m	Heat exchanger	0.05	0.57–0.93
$\max(x_{eva-cond})$, m	Heat exchanger	1.25	0.57–0.93
$\min(\Delta T_{pp}\|_{eva-cond})$, K	Heat exchanger	0.5	1.42–1.31
$\max(v_{air}\|_{eva-cond})$, m/s	Heat exchanger	40	4.08–3.16
$\max(v_{refr}\|_{eva-cond})$, m/s	Heat exchanger	40	9.79–5.35
$\max(\Delta P_{air}\|_{eva-cond})$, kPa	Heat exchanger	1.5	1.15–0.26
$\max(\Delta P_{refr}\|_{eva-cond})$, kPa	Heat exchanger	50	9.23–41.12

The set of optimal values corresponds to the VCC design leading to the minimum fuel weight penalty.

Downloaded by Technische Universiteit Delft on July 17, 2025 | http://arc.aiaa.org | DOI: 10.2514/1.C038093

Acknowledgments

This research was supported by the Dutch Technology Foundation TTW, the Applied Science Division of NWO, the Technology Program of the Ministry of Economic Affairs, and by Aeronamic BV (Grant No. 17091).

References

[1] Bender, D., "Exergy-Based Analysis of Aircraft Environmental Control Systems and Its Integration into Model-Based Design," Ph.D. Thesis, Technische Universität Berlin, Berlin, 2018. https://doi.org/10.14279/DEPOSITONCE-8101

[2] AERO Magazine, 4th Quarter, Boeing, 2007.

[3] Cavalcanti, V., and de Andrade, C., "A Trade-Off Study of a Bleedless and Conventional Air Conditioning Systems," *SAE Brasil Congress and Exhibit*, Paper 2008-36-0001, 2008. https://doi.org/10.4271/2008-36-0001

[4] Ablanque, N., Torras, S., Oliet, C., Rigola, J., and Perez-Segarra, C.-D., "Vapor Compression System Modelica Library for Aircraft ECS," *International Refrigeration and Air Conditioning Conference*, Purdue Univ., West Lafayette, Indiana, 2018, p. 1–10.

[5] Ablanque, N., Torras, S., Rigola, J., and Oliet, C., "Dynamic Model of Vapor Compression Systems for Aircraft Environmental Control Systems," *Journal of Aircraft*, Vol. 61, No. 5, 2024, pp. 1–10. https://doi.org/10.2514/1.C037711

[6] Hu, H., Sun, H., Wu, C., Wang, X., and Lv, Z., "A Steady-State Simulation Model of Supplemental Cooling System Integrated with Vapor Compression Refrigeration Cycles for Commercial Airplane," *Applied Thermal Engineering*, Vol. 166, Feb. 2020, Paper 114692. https://doi.org/10.1016/j.applthermaleng.2019.114692

[7] Xu, Y., Yan, Z., and Xia, W., "A Novel System for Aircraft Cabin Heating Based on a Vapor Compression System and Heat Recovery from Engine Lubricating Oil," *Applied Thermal Engineering*, Vol. 212, July 2022, Paper 118544. https://doi.org/10.1016/j.applthermaleng.2022.118544

[8] Yang, H., and Yang, C., "Derivation and Comparison of Thermodynamic Characteristics of Endoreversible Aircraft Environmental Control Systems," *Applied Thermal Engineering*, Vol. 180, Nov. 2020, Paper 115811. https://doi.org/10.1016/j.applthermaleng.2020.115811

[9] Yang, H., and Yang, C., "Application of Scaling-Endoreversible Thermodynamic Analysis Model to Aircraft Environmental Control System-Methodology Development," *International Journal of Refrigeration*, Vol. 112, April 2020, pp. 90–99. https://doi.org/10.1016/j.ijrefrig.2019.12.006

[10] Vargas, J. V., and Bejan, A., "Integrative Thermodynamic Optimization of the Environmental Control System of an Aircraft," *International Journal of Heat and Mass Transfer*, Vol. 44, No. 20, 2001, pp. 3907–3917. https://doi.org/10.1016/S0017-9310(01)00033-3

[11] Pérez-Grande, I., and Leo, T. J., "Optimization of a Commercial Aircraft Environmental Control System," *Applied Thermal Engineering*, Vol. 22, No. 17, 2002, pp. 1885–1904. https://doi.org/10.1016/S1359-4311(02)00130-8

[12] Leo, T. J., and Pérez-Grande, I., "A Thermoeconomic Analysis of a Commercial Aircraft Environmental Control System," *Applied Thermal Engineering*, Vol. 25, Nos. 2–3, 2005, pp. 309–325. https://doi.org/10.1016/j.applthermaleng.2004.06.011

[13] Sielemann, M., Giese, T., Oehler, B., and Gräber, M., "Optimization of an Unconventional Environmental Control System Architecture," *SAE International Journal of Aerospace*, Vol. 4, No. 2, 2011, pp. 1263–1275. https://doi.org/10.4271/2011-01-2691

Downloaded by Technische Universiteit Delft on July 17, 2025 | http://arc.aiaa.org | DOI: 10.2514/1.C038093

[14] Li, X., Chen, Q., Hao, J. H., Chen, X., and He, K. L., "Heat Current Method for Analysis and Optimization of a Refrigeration System for Aircraft Environmental Control System," *International Journal of Refrigeration*, Vol. 106, Oct. 2019, pp. 163–180. https://doi.org/10.1016/j.ijrefrig.2019.06.004

[15] Duan, Z., Sun, H., Wu, C., and Hu, H., "Multi-Objective Optimization of the Aircraft Environment Control System Based on Component-Level Parameter Decomposition," *Energy*, Vol. 245, April 2022, Paper 123330. https://doi.org/10.1016/j.energy.2022.123330

[16] Giuffré, A., Ascione, F., De Servi, C., and Pini, M., "Data-Driven Modeling of High-Speed Centrifugal Compressors for Aircraft Environmental Control Systems," *International Journal of Refrigeration*, Vol. 151, July 2023, pp. 354–369. https://doi.org/10.1016/j.ijrefrig.2023.03.019

[17] Ascione, F., Colonna, P., and De Servi, C., "Integrated Design Optimization Method for Novel Vapour-Compression-Cycle-Based Environmental Control Systems," *Applied Thermal Engineering*, Vol. 236, Jan. 2024, pp. 121–261. https://doi.org/10.1016/j.applthermaleng.2023.121261

[18] Schweiger, G., Nilsson, H., Schoeggl, J., Birk, W., and Posch, A., "Modeling and Simulation of Large-Scale Systems: A Systematic Comparison of Modeling Paradigms," *Applied Mathematics and Computation*, Vol. 365, Jan. 2020, Paper 124713. https://doi.org/10.1016/j.amc.2019.124713

[19] Giuffré, A., Colonna, P., and Pini, M., "The Effect of Size and Working Fluid on the Multi-Objective Design of High-Speed Centrifugal Compressors," *International Journal of Refrigeration*, Vol. 143, Nov. 2022, pp. 43–56. https://doi.org/10.1016/j.ijrefrig.2022.06.023

[20] Giuffré, A., Colonna, P., and Pini, M., "Design Optimization of a High-Speed Twin-Stage Compressor for Next-Gen Aircraft Environmental Control System," *Journal of Engineering for Gas Turbines and Power*, Vol. 145, No. 3, 2023, Paper 031017. https://doi.org/10.1115/1.4056022

[21] Heath, E. A., "Amendment to the Montreal Protocol on Substances That Deplete the Ozone Layer (Kigali Amendment)," *International Legal Materials*, Vol. 56, No. 1, 2017, pp. 193–205. https://doi.org/10.1017/ilm.2016.2

[22] McLinden, M. O., and Huber, M. L., "(R)Evolution of Refrigerants," *Journal of Chemical & Engineering Data*, Vol. 65, No. 9, 2020, pp. 4176–4193. https://doi.org/10.1021/acs.jced.0c00338

[23] Planès, T., Habrard, V., Delbecq, S., Pommier-Budinger, V., and Benard, E., "Thermal Management System Models for Overall Aircraft Design," *AIAA Aviation 2021 Forum*, AIAA Paper 2021-2428, 2021. https://doi.org/10.2514/6.2021-2428

[24] 86002: Drag and Pressure Recovery Characteristics of Auxiliary Air Inlets at Subsonic Speeds, ESDU, 2004.

[25] Shah, R. K., and Sekulić, D. P., "8.3 Plate-Fin Heat Exchangers," *Fundamentals of Heat Exchanger Design*, Wiley, Hoboken, NJ, 2003, pp. 574–585.

[26] Joshi, H. M., and Webb, R. L., "Heat Transfer and Friction in the Offset Stripfin Heat Exchanger," *International Journal of Heat and Mass Transfer*, Vol. 30, No. 1, 1987, pp. 69–84. https://doi.org/10.1016/0017-9310(87)90061-5

[27] Manglik, R. M., and Bergles, A. E., "Heat Transfer and Pressure Drop Correlations for the Rectangular Offset Strip Fin Compact Heat Exchanger," *Experimental Thermal and Fluid Science*, Vol. 10, No. 2, 1995, pp. 171–180. https://doi.org/10.1016/0894-1777(94)00096-Q

[28] Shah, R. K., and Sekulić, D. P., "Chapter 9—Heat Exchanger Design Procedures," *Fundamentals of Heat Exchanger Design*, Wiley, Hoboken, NJ, 2003, pp. 608–617.

[29] Kays, W. M., and London, A. L., *Compact Heat Exchangers*, 3rd ed., McGraw-Hill, New York, 1984.

[30] Pangborn, H., Alleyne, A. G., and Wu, N., "A Comparison Between Finite Volume and Switched Moving Boundary Approaches for Dynamic Vapor Compression System Modeling," *International Journal of Refrigeration*, Vol. 53, May 2015, pp. 101–114. https://doi.org/10.1016/j.ijrefrig.2015.01.009

[31] Lemmon, E. W., Bell, I. H., Huber, M. L., and McLinden, M. O., "NIST Standard Reference Database 23: Reference Fluid Thermodynamic and Transport Properties-REFPROP," Ver. 10.0, National Inst. of Standards and Technology, 2018, https://www.nist.gov/srd/refprop.

[32] Chang, Y.-J., and Wang, C.-C., "A Generalized Heat Transfer Correlation for Louver Fin Geometry," *International Journal of Heat and Mass Transfer*, Vol. 40, No. 3, 1997, pp. 533–544. https://doi.org/10.1016/0017-9310(96)00116-0

[33] Kandlikar, S. G., "A General Correlation for Saturated Two-Phase Flow Boiling Heat Transfer Inside Horizontal and Vertical Tubes," *Journal of Heat Transfer*, Vol. 112, No. 1, 1990, pp. 219–228. https://doi.org/10.1115/1.2910348

[34] Shah, M., "A General Correlation for Heat Transfer During Film Condensation Inside Pipes," *International Journal of Heat and Mass Transfer*, Vol. 22, No. 4, 1979, pp. 547–556. https://doi.org/10.1016/0017-9310(79)90058-9

[35] Yadav, M. S., Giri, S. A., and Momale, V. C., "Sizing Analysis of Louvered Fin Flat Tube Compact Heat Exchanger by Genetic Algorithm," *Applied Thermal Engineering*, Vol. 125, Oct. 2017, pp. 1426–1436. https://doi.org/10.1016/j.applthermaleng.2017.07.119

[36] Kim, M.-H., and Bullard, C. W., "Air-Side Thermal Hydraulic Performance of Multi-Louvered Fin Aluminum Heat Exchangers," *International Journal of Refrigeration*, Vol. 25, No. 3, 2002, pp. 390–400. https://doi.org/10.1016/S0140-7007(01)00025-1

[37] Kast, W., Nirschl, H., Gaddis, E. S., Wirth, K.-E., and Stichlmair, J., "L1.1 Pressure Drop in Single Phase Flow," *VDI Heat Atlas*, 2nd ed., 2010, pp. 1053–1116. https://doi.org/10.1007/978-3-540-77877-6

[38] Schmidt, J., and Friedel, L., "Two-Phase Pressure Drop Across Sudden Contractions in Duct Areas," *International Journal of Multiphase Flow*, Vol. 23, No. 2, 1997, pp. 283–299. https://doi.org/10.1016/S0301-9322(96)00056-0

[39] Kim, M. H., and Bullard, C. W., "Performance Evaluation of a Window Room Air Conditioner with Microchannel Condensers," *Journal of Energy Resources Technology*, Vol. 124, No. 1, 2002, pp. 47–55. https://doi.org/10.1115/1.1446072

[40] Tiainen, J., Jaatinen-Värri, A., Grönman, A., Sallinen, P., Honkatukia, J., and Hartikainen, T., "Validation of the Axial Thrust Estimation Method for Radial Turbomachines," *International Journal of Rotating Machinery*, Vol. 2021, Feb. 2021, pp. 1–18. https://doi.org/10.1155/2021/6669193

[41] Eckardt, D., "Instantaneous Measurements in the Jet-Wake Discharge Flow of a Centrifugal Compressor Impeller," *Journal of Engineering for Gas Turbines and Power*, Vol. 97, No. 3, 1975, pp. 337–345. https://doi.org/10.1115/1.3445999

[42] Eckardt, D., "Detailed Flow Investigations Within a High-Speed Centrifugal Compressor Impeller," *Journal of Fluids Engineering, Transactions of the ASME*, Vol. 98, No. 3, 1976, pp. 390–399. https://doi.org/10.1115/1.3448334

[43] Eckardt, D., "Investigation of the Jet-Wake Flow of a Highly-Loaded Centrifugal Compressor Impeller," Ph.D. Thesis, RWTH Aachen Univ., Germany, 1977.

[44] Japikse, D., "A Critical Evaluation of Three Centrifugal Compressors with Pedigree Data Sets: Part 5-Studies in Component Performance," *Journal of Turbomachinery*, Vol. 109, No. 1, 1987, pp. 1–9. https://doi.org/10.1115/1.3262064

[45] Schiffmann, J., and Favrat, D., "Experimental Investigation of a Direct Driven Radial Compressor for Domestic Heat Pumps," *International Journal of Refrigeration*, Vol. 32, No. 8, 2009, pp. 1918–1928. https://doi.org/10.1016/j.ijrefrig.2009.07.006

[46] Schiffmann, J., and Favrat, D., "Design, Experimental Investigation and Multi-Objective Optimization of a Small-Scale Radial Compressor for Heat Pump Applications," *Energy*, Vol. 35, No. 1, 2010, pp. 436–450. https://doi.org/10.1016/j.energy.2009.10.010

[47] Kirkby, S., Buchanan, J., Wright, J., Boin, P., Urbanczyk, A., and Boyd, M., "CadQuery, Release 2," 2022, https://github.com/CadQuery/cadquery/.

[48] Van Der Geest, M., Polinder, H., Ferreira, J. A., and Christmann, M., "Power Density Limits and Design Trends of High-Speed Permanent Magnet Synchronous Machines," *IEEE Transactions on Transportation Electrification*, Vol. 1, No. 3, 2015, pp. 266–276. https://doi.org/10.1109/TTE.2015.2475751

[49] Saari, J., "Friction Losses and Heat Transfer in High-Speed Electrical Machines," Helsinki Univ. of Technology TR 50, Helsinki, Dec. 1996.

[50] Giuffré, A., Colonna, P., and De Servi, C., "Dynamic Thermal Model of Passenger Aircraft for the Estimation of the Cabin Cooling and Heating Requirements," *Applied Thermal Engineering*, Vol. 244, May 2024, Paper 122641. https://doi.org/10.1016/j.applthermaleng.2024.122641

[51] Blank, J., and Deb, K., "Pymoo: Multi-Objective Optimization in Python," *IEEE Access*, Vol. 8, 2020, pp. 89,497–89,509. https://doi.org/10.1109/ACCESS.2020.2990567

[52] Deb, K., Pratap, A., Agarwal, S., and Meyarivan, T., "A Fast and Elitist Multiobjective Genetic Algorithm: NSGA-II," *IEEE Transactions on*

Evolutionary Computation, Vol. 6, No. 2, 2002, pp. 182–197. https://doi.org/10.1109/4235.996017

[53] *Aircraft Fuel Weight Penalty due to Air Conditioning*, SAE, June 2004. https://doi.org/10.4271/AIR1168/8

[54] Kim, D., Ziviani, D., Braun, J. E., and Groll, E. A., "A Moving Boundary Modeling Approach for Heat Exchangers with Binary Mixtures," *Energy Procedia*, Vol. 129, Sept. 2017, pp. 466–473. https://doi.org/10.1016/j.egypro.2017.09.161

[55] Deng, H., Rossato, M., Fernandino, M., and Del Col, D., "A New Simplified Model for Condensation Heat Transfer of Zeotropic Mixtures Inside Horizontal Tubes," *Applied Thermal Engineering*, Vol. 153, May 2019, pp. 779–790. https://doi.org/10.1016/j.applthermaleng.2019.02.128

[56] Zhang, J., Mondejar, M. E., and Haglind, F., "General Heat Transfer Correlations for Flow Boiling of Zeotropic Mixtures in Horizontal Plain Tubes," *Applied Thermal Engineering*, Vol. 150, March 2019, pp. 824–839. https://doi.org/10.1016/j.applthermaleng.2019.01.036

B. Thompson
Associate Editor

Downloaded by Technische Universiteit Delft on July 17, 2025 | http://arc.aiaa.org | DOI: 10.2514/1.C038093